Journal of Theoretical Biology 301 (2012) 122–140

Contents lists available at SciVerse ScienceDirect

Journal of Theoretical Biology

journal homepage: www.elsevier.com/locate/yjtbi

Patient-calibrated agent-based modelling of ductal carcinoma in situ (DCIS): From microscopic measurements to macroscopic predictions of clinical progression

Paul Macklin [a,*,1,2], Mary E. Edgerton [b], Alastair M. Thompson [b,c], Vittorio Cristini [d,2]

[a] Center for Applied Molecular Medicine, Keck School of Medicine, University of Southern California, Los Angeles, CA, USA
[b] M.D. Anderson Cancer Center, Houston, TX, USA
[c] Department of Surgery and Molecular Oncology, University of Dundee, Dundee, UK
[d] Departments of Pathology & Chemical Engineering, University of New Mexico, Albuquerque, NM, USA

ARTICLE INFO

Article history:
Received 5 January 2011
Received in revised form
31 January 2012
Accepted 1 February 2012
Available online 9 February 2012

Keywords:
Agent-based model
Ductal carcinoma in situ
Patient-specific calibration
Biomechanics
Calcification

ABSTRACT

Ductal carcinoma in situ (DCIS)—a significant precursor to invasive breast cancer—is typically diagnosed as microcalcifications in mammograms. However, the effective use of mammograms and other patient data to plan treatment has been restricted by our limited understanding of DCIS growth and calcification. We develop a mechanistic, agent-based cell model and apply it to DCIS. Cell motion is determined by a balance of biomechanical forces. We use potential functions to model interactions with the basement membrane and amongst cells of unequal size and phenotype. Each cell's phenotype is determined by genomic/proteomic- and microenvironment-dependent stochastic processes. Detailed "sub-models" describe cell volume changes during proliferation and necrosis; we are the first to account for cell calcification.

We introduce the first patient-specific calibration method to fully constrain the model based upon clinically-accessible histopathology data. After simulating 45 days of solid-type DCIS with comedonecrosis, the model predicts: necrotic cell lysis acts as a biomechanical stress relief and is responsible for the linear DCIS growth observed in mammography; the rate of DCIS advance varies with the duct radius; the tumour grows 7–10 mm per year—consistent with mammographic data; and the mammographic and (post-operative) pathologic sizes are linearly correlated—in quantitative agreement with the clinical literature. Patient histopathology matches the predicted DCIS microstructure: an outer proliferative rim surrounds a stratified necrotic core with nuclear debris on its outer edge and calcification in the centre. This work illustrates that computational modelling can provide new insight on the biophysical underpinnings of cancer. It may 1 day be possible to augment a patient's mammography and other imaging with rigorously-calibrated models that help select optimal surgical margins based upon the patient's histopathologic data.

1. Introduction

Ductal carcinoma in situ (DCIS), a type of breast cancer where growth is confined within the breast ductal/lobular units, is the most prevalent precursor to invasive ductal carcinoma (IDC). Breast cancer is the second-leading cause of death in women in the United States. The American Cancer Society predicted that 50,000 new cases of DCIS alone (excluding other pre-invasive cancers such as lobular carcinoma in situ) and 180,000 new cases of IDC would be diagnosed in 2007 (Jemal et al., 2007; American Cancer Society, 2007). Co-existing DCIS is expected in 80% of IDC (Lampejo et al., 1994). While DCIS itself is not life-threatening, it is clinically important because it can be effectively treated, and if left untreated, it has a high probability of progression to IDC (Page et al., 1982; Kerlikowske et al., 2003; Sanders et al., 2005). While the detection and treatment of DCIS have greatly improved over the last few decades, problems persist. DCIS can be difficult to detect by mammography (the principal modality in breast screening) or to distinguish from other aberrant lesions (Venkatesan et al., 2009). This can lead to "false positives" of DCIS and overtreatment, including unnecessary surgery. When excision is warranted, re-surgery is required in 20–50% of cases to fully eliminate all DCIS (Talsma et al., 2011), highlighting difficulties in

* Corresponding author. Tel.: +1 310 701 5785.
E-mail address: Paul.Macklin@usc.edu (P. Macklin).
URL: http://www.MathCancer.org (P. Macklin).
[1] Formerly of: Division of Mathematics, University of Dundee, Dundee, UK.
[2] Formerly of: SBMI, University of Texas Health Science Center, Houston, TX, USA.

0022-5193/$ - see front matter © 2012 Elsevier Ltd. All rights reserved.
doi:10.1016/j.jtbi.2012.02.002

estimating the full DCIS extent from patient imaging (Cheng et al., 1997; Silverstein, 1997; Cabioglu et al., 2007; Dillon et al., 2007). A solid scientific understanding of DCIS progression is required to improve surgical and therapeutic planning.

Open questions on DCIS biology contribute to current uncertainty in clinical practice. How does DCIS progress from a few proliferating cells to detectable lesions potentially including microcalcifications? Can immunohistochemistry (IHC) and histopathology be used to estimate important physiological constants? Can mathematical modelling provide new insight on interpreting these data? What is the relationship between the microcalcifications observed in mammography and tumour morphology? Can we calibrate patient-specific models to limited and noisy histopathologic data, often from only a single time point? These clinically pertinent scientific questions motivate our work.

Mathematical modelling has already seen use in understanding and predicting the growth and dynamics of DCIS. Frank et al. (2003a,b, 2005) and Owen et al. (2004) used continuum models to investigate tumour growth in breast ducts, including the impact of volume loss in the necrotic core, ductal expansion, and the influence of basement membrane (BM) adhesion; this work can be traced to a long history of work (e.g., Ward and King, 1997) that includes matching to experiments. Rejniak (2007), Rejniak and Dillon (2007), Rejniak and Anderson (2008a,b), and Dillon et al. (2008) applied an immersed boundary method to individual polarised cells; their model was able to reproduce several complex DCIS sub-types. Norton et al. (2010) conducted a similar investigation of the relationship between polarised cell adhesion, intraductal pressure, and DCIS morphology in 2D using a lattice-free agent model and were able to produce nontrivial (e.g., cribriform) tumour microstructures. Gatenby et al. (2007), Silva et al. (2010), and Smallbone et al. (2007) investigated the role of hypoxia, glycolysis, and acidosis in DCIS evolution in 2D and 3D using cellular automata (CA) methods by including detailed metabolic sub-models. Mannes et al. (2002) used 2-D CA methods to investigate Pagetoid spread. Bankhead et al. (2007) conducted early 3-D simulations of tumour cell hierarchy using CA techniques. Sontag and Axelrod (2005) combined population-scale models with machine learning techniques and statistical analyses to postulate new hypotheses on DCIS mutation pathways from benign precursors; Enderling et al. (2006, 2007) used continuum and CA methods to study mutations within DCIS and recurrence following radiotherapy. Very recently, Kim et al. (2011) used a detailed agent-based model to study interactions between DCIS cells and stromal cells via TGF-β and EGF signalling; their work included the effects of basement membrane expansion.

All this work has provided a degree of insight into DCIS, but has not fully answered the questions we posed. Typical CA methods cannot accurately model cell mechanics, particularly proliferation by tumour cells when fully surrounded by other cells; such proliferation is regularly observed in DCIS immunohistochemistry. Population-based ordinary differential equation (ODE) models do not account for spatial heterogeneity and cannot investigate the impact of heterogeneous mechanics, substrate transport, and their interaction. To date, none have modelled calcification, and existing necrosis sub-models have not considered the effects of cell swelling and lysis; many prevalent models ignore necrosis. The work by Norton et al. (2010) shows promise, but it has yet to predict tumour biophysics as *emergent phenomena* because it imposed many of its key properties *a priori* as algorithmic rules. The impressive morphological model of Rejniak and colleagues faces computational limits when applied to large numbers of cells. Continuum models can overcome these limits, but calibration to molecular- and cell-scale data is not straightforward (Macklin et al., 2010b). To our knowledge, there has been no prior patient-specific calibration to the proliferative and apoptotic indices generally measured in breast biopsies at any scale of modelling for DCIS (or for any type of cancer).

Modelling approach and advances: We presently develop a lattice-free, agent-based cell model that can be applied to many problems, exemplified by DCIS. Cells (agents) are modelled as physical objects that exchange and respond to adhesive, repulsive, and motile forces that determine their motion; essential molecular biology is incorporated through carefully-chosen constitutive relations. Cell–cell and cell–BM interaction mechanics are modelled using potential functions that account for finite interaction distances, uncertainty in cell morphology and position, and interaction between cells of variable sizes and types. We introduce a level set formulation of the basement membrane morphology that provides a generalised framework for the exchange of forces between discrete cell objects and extended macroscopic objects with nontrivial, evolving geometries. Each cell is endowed with a phenotypic state, and phenotypic transitions are governed by exponentially-distributed random variables that depend upon the cell's internal state and the local microenvironment. This modelling choice—a natural extension of constant probability per constant time step models prevalent in today' use—is consistent with experimental biology (e.g., Smith and Martin, 1973), provides a rigorous method to vary the model's probabilities with the microenvironment, allows for variable time step sizes, and lends itself to mathematical analysis.

We include detailed "sub-models" of cell volume change during proliferation and necrosis. Our necrosis model, which includes cell swelling and lysis, is the most biologically detailed to date. We are the first to model and investigate cellular calcification. We couple the agents to the microenvironment by solving reaction-diffusion equations for substrates that are altered by the cells. To make the model predictive, we constrain all major model parameters by surveying a broad swath of the experimental and theoretical biology literature.

We provide the first patient-specific model calibration protocol that estimates the population dynamic and mechanical parameters based upon IHC for proliferation (Ki-67), apoptosis (cleaved Caspase-3), and morphometric measurements from haematoxylin and eosin (H&E) histopathology images *at a single time point*, thus avoiding the inherently inaccurate problem of estimating time derivatives from noisy patient data. To our knowledge, this is the first patient-specific cancer calibration method that is based solely upon measurements that we could reasonably expect from a single patient biopsy. Our calibrated model is capable of making testable, quantitative patient-specific predictions of clinical behaviour (see below). Hence, an additional novelty of our work is that we fully document the process of developing a state-of-the-art agent model that is tailored to cancer biology, fully constraining it with biologically relevant parameter estimates and a first-of-its-kind patient-specific calibration to pathology, and generating clinical predictions that are validated against the clinical literature. A preliminary version of this work appeared in Macklin et al. (2009a,2010a,b); this paper refines the model, improves the calibration, and focuses on significant new results, with in-depth validation and analysis.

Main results: We use our model to study solid-type DCIS with comedonecrosis—a central necrotic core that is associated with more frequent recurrence of DCIS and poorer patient prognosis (Ottesen et al., 2000; Yagata et al., 2003). We calibrate our model to archived tissue data from Edgerton et al. (2011) and verify that the calibrated model successfully replicates our patient input data, thus demonstrating the feasibility of calibrating mathematical models based upon patient histopathologic data from a single time point. Away from the tumour's leading edge, the simulated spatiotemporal dynamics reach a steady state after 7–14 days, consistent with a basic population dynamic model analysis and our prior continuum work (Macklin and Lowengrub, 2007).

Based solely upon calibration to microscopic measurements, we make and test macroscopic biological and clinical predictions. The model predicts that DCIS tumours grow at a constant rate through the duct, in agreement with mammographic data. Necrotic core biomechanics play a key role in this finding: necrotic cell lysis acts as a mechanical stress relief that redirects proliferative cell flux towards the duct centre, rather than along the duct. Due to this mechanism, the model predicts that growth is slowest in large ducts with greater capacity to absorb proliferative flux. The model predicts DCIS growth rates between 7.5 and 10.2 mm/year, in quantitative agreement with published clinical data. While the "mammographic image error"—the distance between the calcification and the leading tumour boundary—increases over clinically relevant times, a DCIS tumour's mammographic size is linearly correlated with its pathologic size; this is supported by the clinical literature. A linear extrapolation of the model-predicted correlation demonstrates an excellent agreement with 87 published patient data points spanning two orders of magnitude.

The model also makes microscopic predictions that match clinical data. Fast necrotic cell lysis at the perinecrotic boundary creates a physical gap between the viable rim and the necrotic core; this phenomenon is frequently observed in patient histopathology. The simulated tumours develop a stratified necrotic core, with increasing pyknosis (nuclear degradation) and calcification towards the duct centre; this is observed in patient histopathology. The model also predicts that calcification increases with distance from the tumour's leading edge. The current model only predicts casting-type calcifications. Hence, we hypothesise that other biophysics—such as heterogeneous adhesive forces, cellular secretions, and degradation of the calcifications over long time scales—must be responsible for other types of calcifications observed in mammograms.

These successful quantitative predictions at the microscopic and macroscopic scales suggest that it may soon be possible to use a well-calibrated simulator to create a patient-specific map between the microcalcification geometry (as observed in mammography) and the actual tumour morphology. This could allow surgeons to more precisely plan DCIS surgical margins while removing less non-cancerous tissue, and could improve targeting of radiotherapy.

Paper organisation: After detailing our agent-based model (Section 2), we apply it to DCIS with comedonecrosis (Section 3). After summarising the computational method (Section 4) and patient-independent parameter estimates (Section 5), we detail our patient-specific calibration protocol (Section 6). After calibrating to archived DCIS patient tissue and verifying the calibration (Section 7), we simulate 45 days of DCIS growth and present our clinical predictions in Section 8, with extensive validation against independent clinical data. Discussion and future directions are found in Section 9.

Supplementary material: We include a sampling of significant agent-based modelling beyond DCIS, model generalisations, and further theoretic discussions. We conduct a volume-averaging analysis (key to the calibration protocol). We include full numerical implementation details and introduce a new open standard for sharing multicell agent-based model simulation data (MultiCellXML). We detail our parameter estimates and further analyse our model calibration. We provide additional simulation results, a full simulation data set with open source tools, and animations. See our dedicated webpage at MathCancer.org.[3]

2. Agent-based cell model

We now fully elaborate a discrete, cell-scale modelling framework that we preliminarily introduced in Macklin et al. (2009a, 2010b). See the Supplementary material for a sampling of major agent-based modelling beyond DCIS, as well as recent reviews (Lowengrub et al., 2010; Macklin et al., 2010b). The model is broadly applicable to the epithelial, stromal, and immune cells involved in carcinoma and sarcoma. Its modular design allows "sub-models" (e.g., molecular signalling) to be expanded, simplified, or outright replaced as necessary. Where possible, we choose simple sub-models and test the model framework's success in recapitulating correct DCIS behaviour.

We attempt to model the mechanics, time duration, and biology of each phenotypic state as accurately as our data allow; this should facilitate calibration to molecular- and cellular data. The agents interact with the microenvironment through coupled partial differential equations governing substrate transport. We use the same model for both cancerous and non-cancerous cells. Functionally, the cells differ primarily in the values of their proliferation, apoptosis, and other parameters; this is analogous to the downstream effects of altered oncogenes and tumour suppressor genes (Hanahan and Weinberg, 2000).

In this work, cells are not polarised, and we neglect stem cell dynamics; this is readily added by including a lineage model with each cell agent. Thus, we focus on the tumour growth dynamics, rather than initiation. We do not model cell morphology, but rather total, nuclear, and cytoplasmic volume. Where cell morphology is necessary, we approximate it as spherical, similarly to Ramis-Conde et al. (2008a,b). This approximation is further discussed in Section 2.1. Basement membranes are modelled using level set functions (Section 2.2), which could model BM deformations (Macklin et al., 2010b).

2.1. Physical characteristics and mechanics

We endow each cell with a position $\mathbf{x}$, velocity $\mathbf{v}$, total volume V, cytoplasmic volume V_C, and nuclear volume V_N. We assume that $\mathbf{x}$ and $\mathbf{v}$ are at the cell's centre of mass and volume. While we do not track the cell morphology, we find the equivalent cell and nuclear radii (respectively R and R_N) via

$$V = \tfrac{4}{3}\pi R^3, \quad V_N = \tfrac{4}{3}\pi R_N^3. \tag{1}$$

See Fig. 1 left. For simplicity, we assume V_N is fixed throughout the cell cycle. Each cell has a maximum adhesion interaction distance $R_A \geq R$, which we use to express several effects. Because cells are deformable, they can stretch beyond R to maintain or create adhesive bonds. As we do not explicitly track the cell morphology, there is inherent uncertainty as to maximum extent of the cell boundary relative to its centre of mass; R_A needs to be sufficiently large to account for this. This effect is increased by random actin polymerisation/depolymerisation dynamics, which serve to randomly perturb the cell boundary (Gov and Gopinathan, 2006). See Fig. 1: right.

The cells are allowed to partly overlap to account for cell deformation (Fig. 1: right). We model the relative rigidity of the nucleus (relative to the cytoplasm) by introducing increased mechanical resistance to compression at a distances less than R_N from the cell centre; see Sections 2.3.1 and 2.3.2. Note that as $R_N \uparrow R$ (most of the cell resists compression) or $R_A \downarrow R$ (cells cannot deform to maintain adhesive contact), the cells behave like a granular material.

2.2. Basement membrane morphology

Let us denote the epithelium and lumen (the intraductal space when applied to DCIS) by Ω and the basement membrane by $\partial\Omega$. We represent $\partial\Omega$ implicitly with an auxiliary signed distance

[3] http://www.MathCancer.org/JTB_DCIS_2012

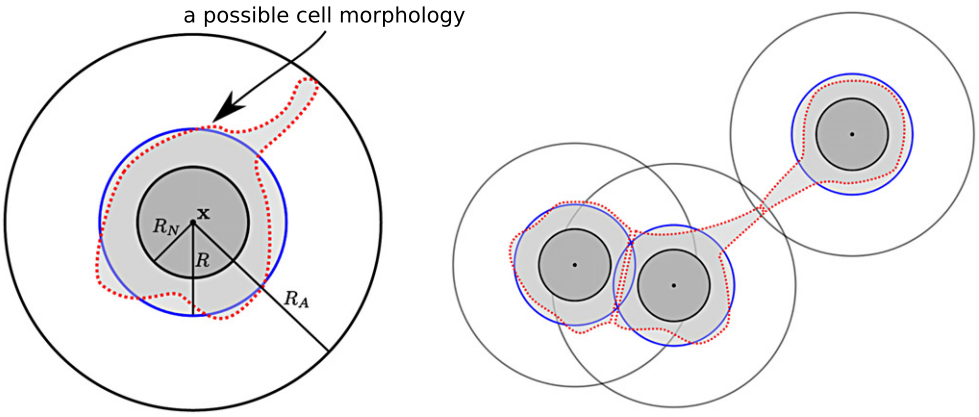

Fig. 1. *Cell morphology and mechanics*: *Left*: we track the cell volume V and nuclear volume V_N (with equivalent spherical radii R and R_N, as labelled here); pale grey denotes the cytoplasm (V_C), and the darker grey denotes the nucleus (V_N). The unknown cell morphology (one possible realisation given as a dashed red curve) has an equivalent spherical morphology (solid blue curve). R_A is the maximum adhesive interaction distance. *Right*: we account for uncertainty in the cell morphology by allowing the equivalent radii to overlap (left two cells), and by allowing adhesive contact beyond their equivalent radii (right two cells). (For interpretation of the references to colour in this figure legend, the reader is referred to the web version of this article.)

function d (a *level set function*) satisfying

$$d(\mathbf{x}) > 0, \quad \mathbf{x} \in \Omega,$$

$$d(\mathbf{x}) = 0, \quad \mathbf{x} \in \partial\Omega,$$

$$d(\mathbf{x}) < 0, \quad \mathbf{x} \notin \overline{\Omega} = \Omega \cup \partial\Omega. \tag{2}$$

Additionally, $|\nabla d| \equiv 1$. This formulation can describe arbitrary BM geometries such as branch points in breast duct tree structures. The normal vector $\mathbf{n}$ to the BM surface (oriented into the epithelium) is $\mathbf{n} = \nabla d$, and $\nabla \cdot \mathbf{n}$ gives the mean geometric curvature of the BM. This implicit representation is well-suited to describing a moving BM as it is deformed by mechanical stresses (e.g., due to proliferating tumour cells, as in Ribba et al., 2006). See Macklin and Lowengrub (2005, 2006, 2007, 2008), Frieboes et al. (2007), and Macklin et al. (2009b) where we used this method to describe moving tumour boundaries.

2.3. Forces acting upon the cells

Cells adhere to other cells (various cell–cell adhesion mechanisms: $\mathbf{F}_{cca}$), the extracellular matrix (cell–ECM adhesion: $\mathbf{F}_{cma}$), and the basement membrane (cell–BM adhesion: $\mathbf{F}_{cba}$). Cells resist compression by other cells (cell–cell repulsion: $\mathbf{F}_{ccr}$). The BM resists its penetration and deformation by cells (cell–BM repulsion: $\mathbf{F}_{cbr}$). Motile cells experience a net locomotive force $\mathbf{F}_{loc}$, and moving cells experience a drag force $\mathbf{F}_{drag} = -v\mathbf{v}_i$ by the luminal and interstitial fluids. See Fig. 2. We neglect any interstitial fluid pressure; this is equivalent to assuming the free flow of water, similarly to current continuum-scale mixture models (e.g., as in Wise et al., 2008). Newton's second law gives the balance of forces acting on cell agent i

$$m_i \dot{\mathbf{v}}_i = \overbrace{\sum_{\substack{j=1 \\ j \neq i}}^{N(t)} (\mathbf{F}^{ij}_{cca} + \mathbf{F}^{ij}_{ccr})}^{\text{cell–cell interactions}} + \overbrace{\mathbf{F}^{i}_{cba} + \mathbf{F}^{i}_{cbr}}^{\text{cell–BM interactions}} + \overbrace{\mathbf{F}^{i}_{cma} + \mathbf{F}^{i}_{drag}}^{\text{cell–medium interactions}} + \mathbf{F}^{i}_{loc}. \tag{3}$$

Here, $N(t)$ is the number of agents in the simulation at time t. The force terms are state-, time-, and microenvironment-dependent; apply to live and dead cell agents; and are governed by individual biological constitutive laws. We set $\mathbf{F}_{loc} = \mathbf{0}$ to focus on the adhesive and repulsive forces. We set $\mathbf{F}_{cma} = \mathbf{0}$ in any lumen; see the Supplementary material for a more general form.

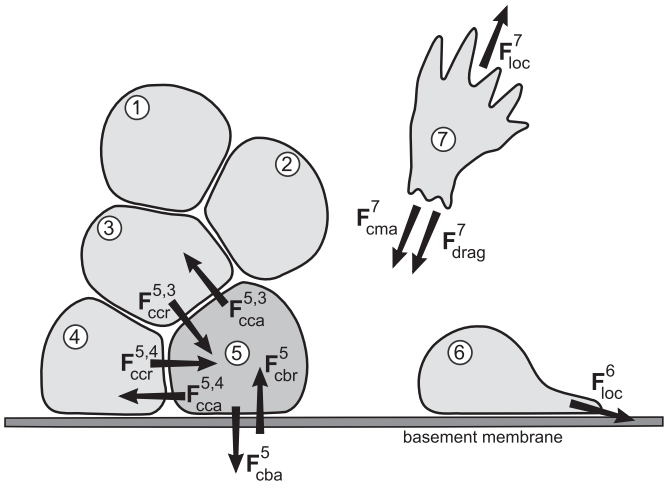

Fig. 2. *Agent model forces*: on Cell 5, find labelled the cell–cell adhesive ($\mathbf{F}^{5j}_{cca}$) and repulsive ($\mathbf{F}^{5j}_{ccr}$) forces, and the cell–BM adhesive ($\mathbf{F}^{5}_{cba}$) and repulsive ($\mathbf{F}^{5}_{cbr}$) forces. We label the net cell locomotive force $\mathbf{F}^{i}_{loc}$ for Cell 6 (undergoing motility along the BM) and Cell 7 (undergoing motility within the ECM). We show the cell–ECM adhesive force ($\mathbf{F}^{7}_{cma}$) and fluid drag ($\mathbf{F}^{7}_{drag}$) for Cell 7. An earlier version of this figure appeared in advance in Macklin et al. (2009a, 2010b).

2.3.1. A simple family of potential functions

As in Drasdo et al. (1995), Drasdo and Höhme (2003, 2005), Drasdo (2005), Ramis-Conde (2008a,b), and Byrne and Drasdo (2009), we model cell–cell biomechanical interactions with potential functions (φ for adhesion; ψ for mechanical resistance/repulsion). We define φ and ψ by their gradients; the forms below are updated from Macklin et al. (2009a, 2010a,b). See Byrne and Drasdo (2009) for a good discussion on modelling cell–cell interactions with potential functions. Ramis-Conde et al. (2008a,b) recently tied potential functions to detailed models of E-cadherin/β-catenin dynamics.

Let R_A be the maximum adhesive interaction distance. For any $n \in \mathbb{N}$, define

$$\nabla\varphi(\mathbf{r}; R_A, n) = \begin{cases} \left(1 - \dfrac{|\mathbf{r}|}{R_A}\right)^{n+1} \dfrac{\mathbf{r}}{|\mathbf{r}|}, & 0 \le |\mathbf{r}| \le R_A \\ \mathbf{0} & \text{else.} \end{cases} \tag{4}$$

Note that $\nabla\varphi$ has compact support, to model the finite interaction distance between cells. The baseline case $n = 0$ is a linear ramping

to the maximum force when $|\mathbf{r}|=0$. For $n>0$, φ tapers off smoothly.

Similarly, if m is a fixed nonnegative integer, R_N is the nuclear radius, R is the cell's radius, and $M \geq 1$ is the cell's maximum repulsive force, define

$$\nabla\psi(\mathbf{r};R_N,R,M,m)=\begin{cases}-\left(c\dfrac{|\mathbf{r}|}{R_N}+M\right)\dfrac{\mathbf{r}}{|\mathbf{r}|}, & 0\leq|\mathbf{r}|\leq R_N\\ -\left(1-\dfrac{|\mathbf{r}|}{R}\right)^{m+1}\dfrac{\mathbf{r}}{|\mathbf{r}|}, & R_N\leq|\mathbf{r}|\leq R\\ \mathbf{0} & \text{else,}\end{cases} \tag{5}$$

where

$$c=\left(\left(1-\frac{R_N}{R}\right)^{m+1}-M\right). \tag{6}$$

As with φ, ψ and its derivatives have compact support; this models the fact that cells only repel one another when they are in physical contact. We make ψ linear in the nuclear region (with $M \geq 1$) to model a stiffer material and allow the nuclear and cytoskeletal mechanics to be specified independently.

Although it is not necessary for our model, we can obtain φ and ψ by directly integrating $\nabla\varphi$ and $\nabla\psi$ with respect to $|\mathbf{x}|$ and setting $\varphi \equiv 0$ on $|\mathbf{x}|=R_A$ and $\psi \equiv 0$ on $|\mathbf{x}|=R$. In Fig. 3, we plot a linear combination of φ and ψ (left) and $\nabla\varphi$ and $\nabla\psi$ (right) that illustrates their use in the forces below.

2.3.2. *Cell–cell adhesion* ($\mathbf{F}_{cca}$) *and repulsion* ($\mathbf{F}_{ccr}$)

Adhesion receptors on a cell's surface bond with adhesive ligands (target molecules) on nearby cells. Hence, the strength of the adhesive force between the cells is (to first order) proportional to the product of the receptor and ligand expressions. The adhesion strength increases as the cells are drawn more closely together, bringing more surface area (and receptor–ligand pairs) into direct contact. We model the force imparted by cell j on cell i by

$$\mathbf{F}_{cca}^{ij}=-c_{cca}f_{i,j}\nabla\varphi(\mathbf{x}_j-\mathbf{x}_i;R_A^i+R_A^j,n_{cca}), \tag{7}$$

where $f_{i,j}$ describes the specific molecular biology of the adhesion, R_A^i is cell i's maximum adhesion interaction distance, and c_{cca} is constant. Note that this form takes into account the deformability of both cells by using $R_A^i+R_A^j$.

In homophilic adhesion (e.g., epithelial cell adhesion by E-cadherin (Panorchan et al., 2006)), adhesion receptors $\mathcal{E}$ bond with identical ligands $\mathcal{E}$. Hence

$$f_{i,j}=\mathcal{E}_i\mathcal{E}_j, \tag{8}$$

where $\mathcal{E}_i$ is cell i's (nondimensionalised) $\mathcal{E}$ receptor expression.

Calcite crystals in partly- and wholly-calcified necrotic cells remain strongly bonded in microcalcifications. We model this as homophilic cell–cell adhesion. If C_i is the nondimensional degree of calcification (see Section 2.5.4), then the general homophilic cell–cell adhesive form is

$$f_{i,j}=\mathcal{E}_i\mathcal{E}_j+C_iC_j. \tag{9}$$

Note that $\mathcal{E}_i$ and C_i are time- and state-dependent: $C_i=0$ in non-necrotic cells; $\mathcal{E}_i$ is degraded and C_i increases in necrotic cells, allowing simultaneous E-cadherin- and calcite-based adhesion during necrosis (Section 2.5.4).

Cells resist compression by other cells due to the structure of their cytoskeletons, the incompressibility of their cytoplasm, and the surface tension of their membranes. We introduce a cell–cell repulsive force that is zero when cells are just touching, and increases rapidly as the cells are pressed together, particularly when their nuclei are in close proximity. We model $\mathbf{F}_{ccr}$ by

$$\mathbf{F}_{ccr}^{ij}=-c_{ccr}\nabla\psi(\mathbf{x}_j-\mathbf{x}_i;R_N^i+R_N^j,R_i+R_j,M,n_{ccr}), \tag{10}$$

where c_{ccr} is a constant, R_N^i and R_i are cell i's nuclear radius and radius, respectively, and M and n_{ccr} are described above.

2.3.3. *Cell–BM adhesion* ($\mathbf{F}_{cba}$) *and repulsion* ($\mathbf{F}_{cbr}$)

Integrin molecules on the cell surface form bonds with specific ligands $\mathcal{L}_B$ (generally laminin and fibronectin, Butler et al., 2008) on the basement membrane (with density $0<B<1$). We assume that $\mathcal{L}_B$ is distributed proportionally to the (nondimensional) BM density B. Hence, the strength of the cell–BM adhesive force is proportional to its integrin surface receptor expression and B. Furthermore, the strength of the adhesion increases as the cell approaches the BM, bringing more cell adhesion receptors in contact with their ligands on the BM. We model this adhesive

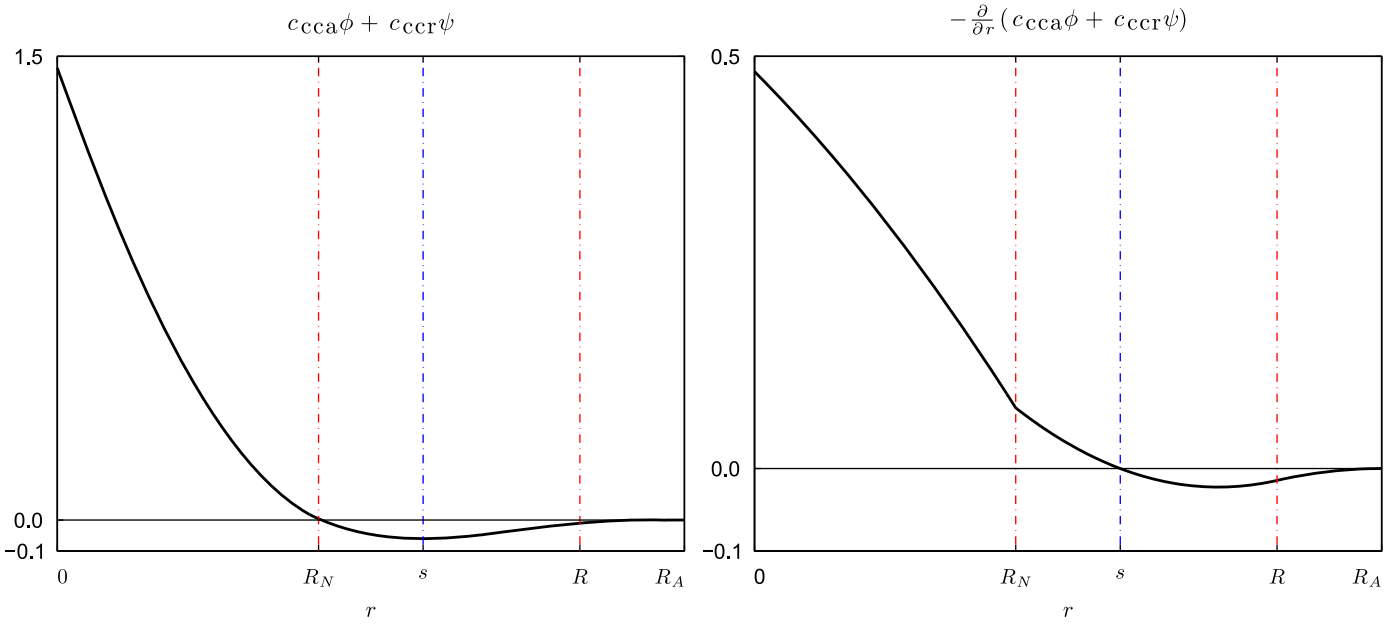

Fig. 3. *Potential functions and derivatives* for $m=n=1$, $M=1$, $R=10$, $R_A=12$, $R_N=5$, $c_{ccr}=1$, and $c_{cca}=0.5184$; $s=7$ is the equilibrium spacing between two interacting cells, where $-\nabla(c_{ccr}\psi+c_{cca}\varphi)=\mathbf{0}$. c_{ccr} and c_{cca} are defined in the following sections. *Left*: $c_{ccr}\psi+c_{cca}\varphi$. *Right*: $-(\partial/\partial r)(c_{ccr}\psi+c_{cca}\varphi)$.

force on cell i by

$$\mathbf{F}^i_{\mathrm{cba}} = -c_{\mathrm{cba}}\mathcal{I}_{\mathrm{B},i}B\nabla\varphi(d(\mathbf{x}_i)\mathbf{n}(\mathbf{x}_i);R^i_{\mathrm{A}},n_{\mathrm{cba}}), \tag{11}$$

where c_{cba} is a constant, d is the distance to the basement membrane, $\mathbf{n}$ is normal to the basement membrane (see Section 2.2), n_{cba} is as described above, and R^i_{A} and $\mathcal{I}_{\mathrm{B},i}$ are cell i's maximum adhesion interaction distance and (nondimensionalised) integrin receptor expression, respectively. Setting the maximum interaction distance to R^i_{A} is consistent with our modelling simplification that the basement membrane is non-deformable. We model the BM's resistance to deformation and penetration by cells and debris by

$$\mathbf{F}^i_{\mathrm{cbr}} = -c_{\mathrm{cbr}}B\nabla\psi(d(\mathbf{x}_i)\mathbf{n}(\mathbf{x}_i;R^i_{\mathrm{N}},R_i,M,n_{\mathrm{cbr}}), \tag{12}$$

where c_{cbr} is a constant, d is the distance to the BM, R^i_{N} and R_i are described earlier, and M and n_{cbr} are described above.

2.4. "Inertialess" assumption

Similarly to Drasdo et al. (1995), Galle et al. (2005), and Ramis-Conde et al. (2008b) and as discussed in Lowengrub et al. (2010), we make the "inertialess" assumption that the forces equilibrate quickly, and so $|m_i\dot{\mathbf{v}}_i| \approx 0$. Hence, we approximate $\sum \mathbf{F} = \mathbf{0}$ and solve for the cell velocity from Eq. (3)

$$\mathbf{v}_i = \frac{1}{v+c_{\mathrm{cma}}\mathcal{I}_{\mathrm{E},i}E}\left(\sum_{\substack{j=1\\ j\neq i}}^{N(t)}(\mathbf{F}^{ij}_{\mathrm{cca}}+\mathbf{F}^{ij}_{\mathrm{ccr}})+\mathbf{F}^i_{\mathrm{cba}}+\mathbf{F}^i_{\mathrm{cbr}}+\mathbf{F}^i_{\mathrm{loc}}\right). \tag{13}$$

This has a convenient interpretation: each term $(1/v+c_{\mathrm{cma}}\mathcal{I}_{\mathrm{E},i}E)\mathbf{F}_{\square}$ is the "terminal" (equilibrium) velocity of the cell when fluid drag, cell–ECM adhesion, and $\mathbf{F}_{\square}$ are the only forces acting upon it. Here, "$\square$" represents any individual force above, e.g., cba, cca, etc., and $N(t)$ is the number of simulated cells at time t. The coefficient $1/(v+c_{\mathrm{cma}}\mathcal{I}_{\mathrm{E},i}E)$ can be directly related to Darcy's law in several tumour models; see the Supplementary material.

2.5. Cell phenotypic states

We endow each agent with a phenotypic state $\mathcal{S}(t)$ in the state space $\{\mathcal{Q},\mathcal{P},\mathcal{A},\mathcal{H},\mathcal{N}\}$ (introduced below). Quiescent cells ($\mathcal{Q}$) are in a "resting state" (G_0, in terms of the cell cycle); this is the "default" state in the framework. We model transitions between cell states as stochastic events governed by exponentially distributed random variables that are linked to the cell's genetic and proteomic state, as well as the microenvironment. These exponentially distributed variables can be regarded as arising from nonhomogeneous Poisson processes; a brief discussion is in the Supplementary material.

For a transition to state $\mathcal{S}_2$ from the current state $\mathcal{S}_1$, and for any interval $(t,t+\Delta t]$, we use the general form

$$\Pr(\mathcal{S}(t+\Delta t)=\mathcal{S}_2\,|\,\mathcal{S}(t)=\mathcal{S}_1) = 1-\exp\left(-\int_t^{t+\Delta t}\alpha_{12}(\mathcal{S},\bullet,\circ)(s)\,ds\right), \tag{14}$$

where $\alpha_{12}(\mathcal{S},\bullet,\circ)(t)$ is the intensity function, $\bullet$ represents the cell's internal (genetic and proteomic) state, and $\circ$ represents the state of the surrounding microenvironment sampled at the cell's position $\mathbf{x}(t)$. Note that for small Δt

$$\Pr(\mathcal{S}(t+\Delta t)=\mathcal{S}_2\,|\,\mathcal{S}(t)=\mathcal{S}_1) = \alpha_{12}(\mathcal{S},\bullet,\circ)(t)\Delta t+\mathcal{O}(\Delta t^2). \tag{15}$$

When α_{12} is constant, we recover (to second order) the commonly-used constant transition probabilities for fixed step sizes Δt; these may be regarded as approximations to our more general model here. This linearisation may be used in numerical implementations for small Δt to improve performance.

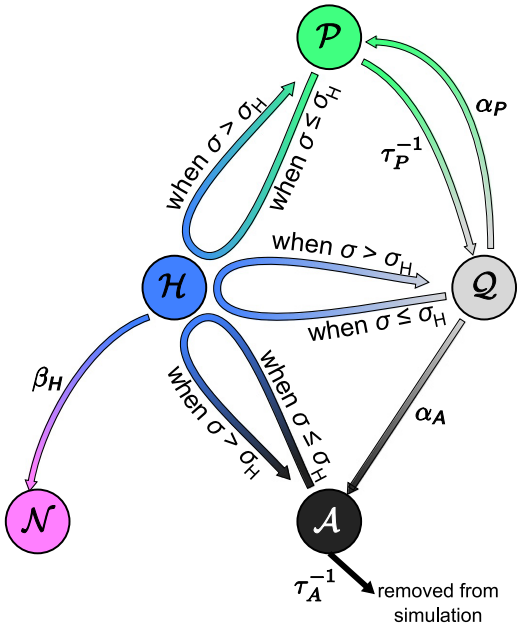

Fig. 4. Phenotypic transition network in the agent-based model, including quiescent ($\mathcal{Q}$), proliferative ($\mathcal{P}$), apoptotic ($\mathcal{A}$), hypoxic ($\mathcal{H}$), and necrotic ($\mathcal{N}$) cells. An earlier version of this figure appeared in advance in Macklin et al. (2010b).

In our phenotypic state space, quiescent cells can become proliferative ($\mathcal{P}$) or apoptotic ($\mathcal{A}$). Non-necrotic cells become hypoxic ($\mathcal{H}$) when oxygen σ drops below a threshold value σ_{H}. Hypoxic cells can recover to their previous state or become necrotic ($\mathcal{N}$). Cell calcification (previously denoted $\mathcal{C}$ in Macklin et al., 2009a, 2010a,b) is included in the necrotic state. See Fig. 4. We include the subcellular scale by varying the transition parameters with the cell's internal state and the local microenvironment.

Cell cycle models have also been used to regulate the $\mathcal{P}\to\mathcal{Q}$ transition (e.g., Abbott et al., 2006; Zhang et al., 2007), and signalling networks have been developed to regulate $\mathcal{Q}\to\{\mathcal{P},\mathcal{A},\mathcal{M}\}$ (where $\mathcal{M}$ is motile) transitions. These can be directly integrated into the agent framework by modifying the stochastic parameters or by outright replacing the exponential random variables with deterministic processes. Excellent examples of agent-based modelling with subcellular signalling components include Chen et al. (2009b,a), Kharait et al. (2007), Wang et al. (2007), and Zhang et al. (2007, 2009).

2.5.1. Proliferation ($\mathcal{P}$)

As suggested by experimental and theoretical work (e.g., Smith and Martin, 1973), quiescent cells enter the proliferative state (i.e., progress from G_0 to S) with a probability that depends upon the microenvironment. We model the probability of a quiescent cell entering the proliferative state in the time interval $(t,t+\Delta t]$ via an exponentially-distributed random variable

$$\Pr(\mathcal{S}(t+\Delta t)=\mathcal{P}\,|\,\mathcal{S}(t)=\mathcal{Q}) = 1-\exp\left(-\int_t^{t+\Delta t}\alpha_{\mathrm{P}}(\mathcal{S},\bullet,\circ)(s)\,ds\right)$$
$$\approx 1-\exp(-\alpha_{\mathrm{P}}(\mathcal{S},\bullet,\circ)(t)\Delta t), \tag{16}$$

where the approximations best hold for small $\alpha_{\mathrm{P}}\Delta t$.

Assuming a correlation between the microenvironmental oxygen level σ (nondimensionalised by the far-field oxygen level in non-diseased, normoxic tissue) and proliferation (see the Supplementary material and the excellent exposition in Silva and

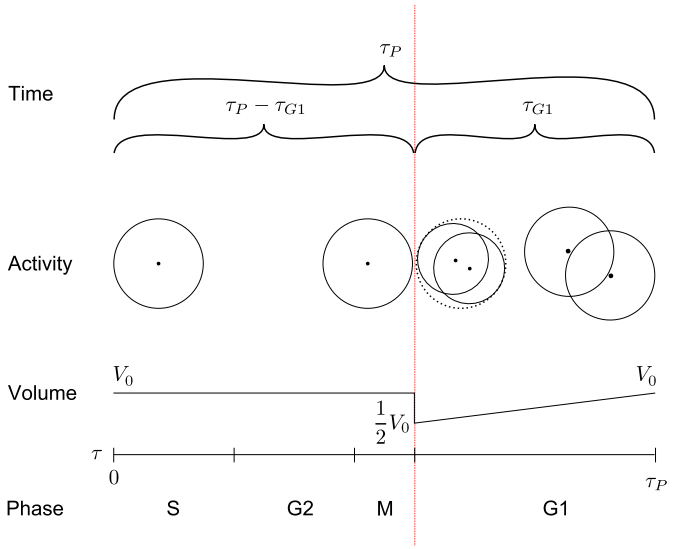

Fig. 5. $\mathcal{P}$ *sub-model*: a cell enters $\mathcal{P}$ from the quiescent state $\mathcal{Q}$, modelling the G_0 to S transition. It then remains in $\mathcal{P}$ until dividing into two identical daughter cells of half volume. The daughter cells also remain in $\mathcal{P}$ until completing G_1 and "maturing" into full-sized cells; thereafter, they enter the "default" state $\mathcal{Q}$.

Gatenby, 2010)), we expect α_P to increase with σ. Hence

$$\alpha_P(\mathcal{S},\sigma,\bullet,\circ)(t) = \overline{\alpha}_P(\bullet,\circ)\left(\frac{\sigma-\sigma_H}{1-\sigma_H}\right), \tag{17}$$

where σ_H is a threshold oxygen value at which cells become hypoxic, and $\overline{\alpha}_P(\bullet,\circ)$ is the cell's $\mathcal{Q}\to\mathcal{P}$ transition rate when $\sigma = 1$ (i.e., in normoxic tissue), which depends upon the cell's genetic profile and proteomic state ($\bullet$) and the local microenvironment ($\circ$). In tumours, low oxygenation is the norm (Gatenby et al., 2007; Smallbone et al., 2007, and so σ is far below 1; typically, $\sigma_H \sim 0.2$ and $\sigma < 0.4$ in the lumen; see the Supplementary material.

For simplicity, we model $\overline{\alpha}_P$ as constant for and specific to each cell type. In Macklin et al. (2010b), we discuss how to incorporate $\bullet$ (i.e., a cell's internal protein expression) and $\circ$ (as sampled by a cell's surface receptors) into α_P through a subcellular molecular signalling model. Note that models have been developed to reduce the proliferation rate in response to mechanical stresses (e.g., Shraiman, 2005); in the context of the model, a cell samples these stresses from continuum-scale variables (i.e., "$\circ$") to reduce α_P.

Once a cell has entered the proliferative state $\mathcal{P}$, it remains in that state until dividing into two identical daughter cells of half volume, which themselves remain in $\mathcal{P}$ until "maturing" into full-sized cells at the end of G_1. Thereafter, the daughter cells are placed in the "default" quiescent state $\mathcal{Q}$ to simulate the transition from G_1 to G_0 (Fig. 5). We now describe these events in greater detail.

Define τ to the elapsed time since the cell entered the cell cycle from $\mathcal{Q}$. Similarly to Ramis-Conde et al. (2008b), we divide the cell cycle (with duration τ_P) into the S–M phases and the G_1 phase (with duration τ_{G1}). While τ_P and τ_{G1} may generally depend upon the microenvironment and the cell's internal state, we currently model them as fixed for any given cell type.

At time $\tau = \tau_P - \tau_{G1}$ (at the end of M), we divide the cell into two identical daughter cells with half the mass and volume of the parent cell. We assume that both daughter cells evenly inherit the parent cell's surface receptor expressions, internal protein expressions, and genetic characteristics (as embodied by the phenotypic state transition parameters). We model the cell's volume V by

$$V(\tau) = \begin{cases} V_0, & 0 \le \tau \le \tau_P - \tau_{G1} \\ \frac{1}{2}V_0\left(1 + \frac{\tau_{G1} + (\tau - \tau_P)}{\tau_{G1}}\right), & \tau_P - \tau_{G1} \le \tau \le \tau_P, \end{cases} \tag{18}$$

where V_0 is the cell's "mature" volume; V_N is fixed through the cycle.

Let R_{parent} be the radius of the parent cell (with position $\mathbf{x}_0$), and $R_{daughter}$ that of the daughter cells (centered $\mathbf{x}_+$ and $\mathbf{x}_-$). Pick $\theta \in [0, 2\pi)$ with uniform distribution. Let $\mathbf{u}_{rand} = (\cos\theta, \sin\theta)$, and position the daughter cells by

$$\mathbf{x}_\pm = \mathbf{x}_0 \pm (R_{parent} - R_{daughter})\mathbf{u}_{rand}. \tag{19}$$

The daughter cells are subsequently pushed apart by cell–cell repulsive forces.

2.5.2. Apoptosis ($\mathcal{A}$)

Apoptotic cells undergo "programmed" cell death in response to signalling events. We model entry into $\mathcal{A}$ as exponentially-distributed with parameter $\alpha_A(\mathcal{S},\bullet,\circ)(t)$. We assume no correlation between apoptosis and oxygen

$$\Pr(\mathcal{S}(t+\Delta t) = \mathcal{A} | \mathcal{S}(t) = \mathcal{Q}) = 1 - \exp\left(-\int_t^{t+\Delta t} \alpha_A(\mathcal{S},\bullet,\circ)(s)\, ds\right), \tag{20}$$

where

$$\alpha_A(\mathcal{S},\bullet,\circ)(t) = \overline{\alpha}_A(\bullet,\circ), \tag{21}$$

and where $\circ$ does not include oxygen σ, but may include other microenvironmental stimuli such as proximity of the BM (anoikis), chemotherapy, or continuum-scale mechanical stresses that increase α_A as in Shraiman (2005). Cells remain in the apoptotic state for a fixed amount of time τ_A; afterward they are removed from the simulation to model phagocytosis of apoptotic bodies. Their previously-occupied volume is made available to the surrounding cells to model the release of the cells' water content after lysis.

2.5.3. Hypoxia ($\mathcal{H}$)

Cells enter the hypoxic state at any time that $\sigma < \sigma_H$. In this paper, we use the simplification that hypoxic cells cannot recover to their previous state, and instead immediately become necrotic ($\beta_H \to \infty$ in Fig. 4). See Macklin et al. (2010b) and the Supplementary material for a more generalised form.

2.5.4. Necrosis (including calcification) ($\mathcal{N}$)

For any cell in the $\mathcal{N}$ state, its surface receptors (particularly E-cadherins and integrins) and subcellular structures degrade, it loses its liquid volume, and calcium is deposited (primarily) in its solid fraction. Let τ denote the elapsed time spent in the necrotic state. Define τ_{NL} to be the length of time for the cell to swell, lyse, and lose its water content, τ_{NS} the time for all surface receptors to become functionally inactive, and τ_C, the time for calcification to occur. We assume that $\tau_{NL} < \tau_{NS} < \tau_C$. In Macklin et al. (2009a) we found that a simplified model (where $\tau_{NL} = \tau_{NS} = \tau_C$) could not reproduce certain morphological aspects of the viable rim-necrotic core interface in breast cancer.

We assume a constant rate of calcification, reaching a radiologically-detectable level at $\tau = \tau_C$. If C is the nondimensional degree of calcification (scaled by the detection threshold), then $C(\tau) = \tau/\tau_C$ for $0 \le \tau \le \tau_C$, and $C(\tau) = 1$ otherwise. We model the degradation of any surface receptor S (scaled by the non-necrotic expression level) by exponential decay with rate constant $\log 100/\tau_{NS}$, so that $S(\tau_{NS}) = 0.01\, S(0)$. We set $S(\tau) = 0$ for $\tau > \tau_{NS}$.

To model the necrotic cell's volume change, let f_{NS} be the maximum percentage increase in the cell's volume (just prior to lysis), and let V_0 be the cell's volume at the onset of necrosis. Then

we model

$$V(\tau) = \begin{cases} V_0\left(1+f_{\mathrm{NS}}\dfrac{\tau}{\tau_{\mathrm{NL}}}\right) & \text{if } 0 \le \tau < \tau_{\mathrm{NL}} \\ V_{\mathrm{N}} & \text{if } \tau_{\mathrm{NL}} < \tau. \end{cases} \tag{22}$$

To model uncertainty in the cell morphology during lysis, we randomly perturb its location $\mathbf{x}$ such that its new radius $R(\tau_{\mathrm{NL}})$ is contained within its swelled radius $R(0)(1+f_{NS})^{1/3}$.

2.6. Dynamic coupling with the microenvironment with upscaling

We integrate the agent model with the microenvironment by introducing field variables for key microenvironmental components (oxygen, growth factors, ECM, etc.) that are governed by continuum equations. These variables affect the cell agents' behaviour as already described; simultaneously, the agents impact the evolution of the continuum variables, as we demonstrate for oxygen transport. At the macroscopic scale, oxygen transport is modelled by

$$\partial\sigma/\partial t = \nabla\cdot(D\nabla\sigma) - \lambda\sigma, \tag{23}$$

where σ is oxygen, D is its diffusion constant, and λ is the (spatiotemporally variable) uptake/decay rate. Suppose that viable (non-necrotic, non-calcified) tumour cells uptake oxygen at a rate λ_{t}, host cells at a rate λ_{h}, and elsewhere oxygen "decays" (by reacting with the molecular landscape) at a low background rate λ_{b}. Suppose that in a small neighbourhood B of $\mathbf{x}$, tumour cells, host cells, and stroma (non-cells), respectively, occupy fractions f_{t}, f_{h}, and f_{b} of B, where $f_{\mathrm{t}}+f_{\mathrm{h}}+f_{\mathrm{b}}=1$. Then $\lambda(\mathbf{x})$ is given by

$$\lambda(\mathbf{x}) \approx f_{\mathrm{t}}\lambda_{\mathrm{t}} + f_{\mathrm{h}}\lambda_{\mathrm{h}} + f_{\mathrm{b}}\lambda_{\mathrm{b}}, \tag{24}$$

i.e., by averaging the uptake rates with weighting according to the tissue composition near $\mathbf{x}$. This is consistent with the uptake rate model by Hoehme and Drasdo (2010), which they based upon the experimental literature.

In numerical implementations, we construct λ at a scale that resolves the cells (mesh size: 1 μm) and upscale it to the computational mesh (mesh size: $0.1\,L = 10$ μm) (see the Supplementary material). Thus, the uptake rate varies with the tumour microstructure, which, in turn, evolves according to substrate availability. We set $\sigma = \sigma_{\mathrm{B}}$ (for constant σ_{B}) where $d \le 0$ model the release of oxygen by a pre-existent vasculature in the stroma. We use Neumann boundary conditions where the lumen intersects the computational boundary.

3. Model application to ductal carcinoma in situ (DCIS)

To model solid-type DCIS, tumour cells are non-polarised (with uniformly-distributed adhesion receptors) and are assumed to ignore E-cadherin signalling for contact inhibition. Tumour cells in the viable rim can be quiescent ($\mathcal{Q}$), apoptotic ($\mathcal{A}$), or proliferative ($\mathcal{P}$). In hypoxic regions ($\sigma < \sigma_{\mathrm{H}}$), cells immediately become necrotic ($\mathcal{N}$), and eventually become calcified. We assume that there is no ECM in the duct lumen ($E \equiv 0$). Cells adhere to cells by E-cadherins, and cell-BM adhesion is between integrins and uniformly-distributed ligands on the BM. For simplicity, we neglect molecular-scale signalling and membrane deformation and degradation, as well as the presence of non-cancerous epithelial cells lining the duct.

For simulation in 2D, consider cells growing in a fluid-filled domain Ω (a rigid-walled duct) of length ℓ and width $2R_{\mathrm{duct}}$. To prevent artifacts (artificial stresses and mechanical tears) that often arise in non-biological corners in computational domains, we "cap" the left edge of the virtual duct with a semicircle of radius R_{duct}. This simulates growth through a partly-filled, densely-packed duct (thereby preventing cell flux out the left boundary), as is the case when DCIS is clinically detected. We model oxygen transport within the duct by Eq. (23) (for constant D), and λ is as discussed above. We set $\partial\sigma/\partial n = 0$ on the righthand side of the duct.

4. Numerical methods

We implement the model using object-oriented ANSI C++, where each agent is an instance of a `Cell` class. Each cell object is endowed with an instance of a `Cell_State` class, which contains the cell phenotypic parameters ($\overline{\alpha}_P$, α_{A}, τ_{P}, etc.), volumes (V_{C},V_{N},V), radii (R_{N},R), maximum interaction distance (R_{A}, recorded as a multiple of R), position $\mathbf{x}$, and velocity $\mathbf{v}$. We discretise microenvironmental field variables (e.g., oxygen σ) on an independent Cartesian mesh with uniform spacing $\Delta x = \Delta y = 0.1L$, where L is the oxygen diffusion length scale. We represent the BM morphology with a level set function, and we use an auxiliary data structure to reduce the computational cost of cell-cell interaction testing and evaluation. The overall computational cost of the algorithm scales linearly in the number of cells (per computational time step). See the Supplementary material for full computational details.

5. Patient-independent parameter estimation

We estimated patient-independent parameters through an extensive search of the theoretical and experimental biology and clinical literature. We summarise those estimates here, which are improved beyond Macklin et al. (2009a, 2010a). See the Supplementary material for full details and references. Note that the quantitative validation results in Section 8 serve to test the adequacy of order-of-magnitude estimates of those parameters that cannot be directly measured.

Cell cycle time τ_{P}:18 h by the modelling literature.

G_1 time τ_{G1}: $\frac{1}{2}\tau_{\mathrm{P}} = 9$ h by the theoretical biology literature.

Apoptosis time τ_{A}: 8.6 h by population dynamic analysis of immunohistochemical stains of terminal ductal lobular units in non-cancerous women in the clinical literature. Estimate accounts for detection shortcomings in TUNEL assay and cleaved Caspase-3 immunohistochemistry.

Necrotic cell lysis time τ_{NL}: 6 h by the experimental literature.

Necrotic cell volume increase f_{NS}: 1.0 by the experimental literature.

Necrotic cell calcification time τ_{C}: 15 days by the clinical and experimental literature, and preliminary simulations.

Oxygen diffusion length scale L: 100 μm by the modelling literature.

Tumour cell oxygen uptake rate λ: 0.1 min^{-1} by the modelling literature and $L = \sqrt{D/\lambda}$.

Oxygen uptake/decay rate for non-viable cells and background λ_{b}: 0.01λ by model simplification.

Hypoxic oxygen threshold σ_{H}: 0.2 by the modelling literature and analysis.

Maximum adhesion interaction distance R_{A}: $1.214\,R$ (R is the equivalent cell radius) by the experimental literature on breast cell deformations.

Cell–cell repulsive force coefficient c_{ccr}: $10.0v$ μm/min by comparing potential functions to experimental literature on

tensional forces applied to magnetic microbeads embedded in cell cytoskeletons.

Cell–BM repulsive force coefficient c_{cbr}: c_{ccr} by model simplification.

Cell–cell adhesion and repulsion potential exponents n_{cca} and n_{ccr}: set to 1 by model simplifications.

Cell–BM adhesion and repulsion potential exponents n_{cba} and n_{cbr}: set to n_{cca} and n_{ccr}, respectively, by model simplification.

M, **the maximum value of** $|\nabla\psi|$: 1 by model simplification.

6. Patient-specific model calibration

We now present a patient-specific calibration protocol for DCIS. The technique can be applied more generally to tumours with clearly visible viable rims; we point out these generalisations wherever possible. The following DCIS patient data are available (full methodological details are given in Edgerton et al., 2011)):

- Average duct radius $\langle R_{duct}\rangle$ and viable rim thickness $\langle T\rangle$, measured on the IHC images. In a tumour spheroid, we would use its radius in place of R_{duct}.
- Average cell density $\langle\rho\rangle$ in the viable rim, calculated by counting nuclei and dividing by the computed viable rim size.
- Average cell nuclear radius R_N.
- Cell confluence f in the viable rim, defined to be the area fraction of the viable region occupied by cell nuclei and cytoplasm.
- Proliferative index PI, measured by staining images for Ki-67 (a nuclear protein marker for cell cycling), and then dividing the total number of Ki-67-positive nuclei by the total number of nuclei in the viable rim.
- Apoptotic index AI, measured by staining for cleaved Caspase-3, an "executioner" caspase reflecting the apoptosis process. As Caspase-3 is a cytosolic protein, we identify and count positive cells by comparing the whole cell staining intensities, and divide the count by the total number of nuclei across the viable rim. We multiply this "raw AI" by a correction factor (8.6/6.6) to obtain a "corrected AI". This accounts for early apoptotic cells that do not stain positive for cleaved Caspase-3; see the Supplementary material.

The patient-specific parameters and their physical meanings are in Table 1.

Duct and cell geometry: We match the simulated duct radius to the mean measured duct radius $\langle R_{duct}\rangle$. We obtain the average (equivalent) cell radius R from the mean viable rim cell density $\langle\rho\rangle$ and measured confluence f (where $0\le f\le 1$) by the relation

$$f=\langle\rho\rangle\pi R^2. \tag{25}$$

We measure the cell nuclear radius R_N in histopathology.

Oxygen: The mean viable rim thickness $\langle T\rangle$ is an indicator of oxygenation to determine the boundary value σ_B. In 2D the steady-state oxygen profile away from the leading edge satisfies

$$0=\begin{cases} D\sigma''-\lambda\sigma, & 0<x<\langle T\rangle,\\ D\sigma''-\Lambda_b\lambda\sigma, & \langle T\rangle<x<\langle R_{duct}\rangle,\end{cases} \tag{26}$$

with the boundary and matching conditions

$$\sigma(0)=\sigma_B,\quad \sigma(\langle T\rangle)=\sigma_H,\quad \sigma'(\langle R_{duct}\rangle)=0, \tag{27}$$

$$D\lim_{x\uparrow\langle T\rangle}\sigma'(x)=D\lim_{x\downarrow\langle T\rangle}\sigma'(x). \tag{28}$$

Here, x is the distance from the duct wall, and $\Lambda_B=\lambda_b/\lambda$. After applying all conditions except $\sigma(0)=\sigma_B$, solving Eq. (26) analytically, and evaluating at $x=0$, we obtain the boundary condition σ_B

$$\sigma_B=\sigma_H\left[\cosh\frac{\langle T\rangle}{L}+\sqrt{\Lambda_b}\tanh\left(\frac{\langle R_{duct}\rangle-\langle T\rangle}{L/\sqrt{\Lambda_b}}\right)\sinh\frac{\langle T\rangle}{L}\right]. \tag{29}$$

Similarly, the mean oxygen value across the viable rim is

$$\langle\sigma\rangle=\sigma_H\frac{L}{\langle T\rangle}\left[\sqrt{\Lambda_b}\tanh\left(\frac{\langle R_{duct}\rangle-\langle T\rangle}{L/\sqrt{\Lambda_b}}\right)\left(\cosh\frac{\langle T\rangle}{L}-1\right)+\sinh\frac{\langle T\rangle}{L}\right]. \tag{30}$$

For tumour spheroids, we would replace $\langle R_{duct}\rangle$ with the mean tumour spheroid radius. For fingering tumours, we would use mean "finger" radius.

Population dynamics: By solving ODEs for PI and AI (Supplementary material) to steady state, given τ_P, τ_A, PI and AI, we obtain $\langle\alpha_P\rangle$ and α_A via

$$\langle\alpha_P\rangle=\left(\frac{1}{\tau_P}(PI+PI^2)-\frac{1}{\tau_A}AI\cdot PI\right)\Big/(1-AI-PI), \tag{31}$$

$$\alpha_A=\left(\frac{1}{\tau_A}(AI-AI^2)+\frac{1}{\tau_P}AI\cdot PI\right)\Big/(1-AI-PI). \tag{32}$$

We calibrate the functional form for α_P by combining this result with the computed mean oxygen in the previous step and solving for $\overline{\alpha}_P$

$$\langle\alpha_P\rangle=\overline{\alpha}_P\left(\frac{\langle\sigma\rangle-\sigma_H}{1-\sigma_H}\right). \tag{33}$$

Cell–cell mechanics: We first estimate the equilibrium spacing s between cell centres. For confluent cells ($f=1$) in non-hypoxic tissue, we determine s by converting the mean density $\langle\rho\rangle$ to an equivalent hexagonal cell packing

$$s=\sqrt{2/(\sqrt{3}\langle\rho\rangle)}. \tag{34}$$

Next, for two cells i and j, we solve for the ratio of the adhesive and repulsive forces that enforces the cell spacing s by equilibrating the cell–cell adhesive and repulsive forces at $r=s$

$$\mathcal{E}_i\mathcal{E}_j\frac{c_{cca}}{c_{ccr}}=\left|\frac{\frac{\partial}{\partial r}\psi(s;R_N^i+R_N^j,R^i+R^j,M,n_{ccr})}{\frac{\partial}{\partial r}\varphi(s;R_A^i+R_A^j,n_{cca})}\right|=\frac{\left(1-\frac{s}{R^i+R^j}\right)^{n_{ccr}+1}}{\left(1-\frac{s}{R_A^i+R_A^j}\right)^{n_{cca}+1}}. \tag{35}$$

If i and j are of the same cell type with identical radii and interaction adhesion distances, and if we set $\mathcal{E}=1$ for both cells,

Table 1
Patient-specific parameters for Patient 100019 for the DCIS model.

Parameter	Physical meaning	Value
R	Cell radius	9.953 μm
R_N	Cell nuclear radius	5.295 μm
σ_B	Oxygen value on the BM	0.263717
$\langle\sigma\rangle$	Mean oxygen level in viable rim	0.221065
$\langle\alpha_P\rangle$	Mean $\mathcal{Q}\to\mathcal{P}$ transition rate	0.013705 h^{-1}
$\overline{\alpha}_P^{-1}$	Mean waiting time prior to $\mathcal{Q}\to\mathcal{P}$ transition when $\sigma=1$	115.27 min
α_A	$\mathcal{Q}\to\mathcal{A}$ transition rate	0.00127128 h^{-1}
s	Cell spacing	18.957 μm
c_{cca}	Cell–cell adhesive force coefficient	$0.0488836c_{ccr}$
c_{cba}	Cell–BM adhesive force coefficient	$10c_{cca}$

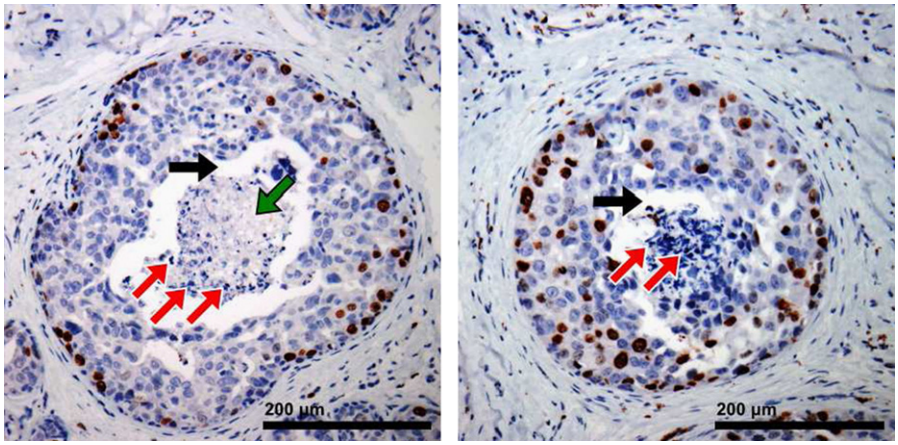

Fig. 6. *Ki-67 immunohistochemistry of two DCIS duct cross sections* in case 100019. Nuclei of cycling cells ($\mathcal{P}$: S, G_2, M, and G_1) stain dark red, while nuclei of non-cycling cells ($\mathcal{Q}$: G_0) counterstain blue. In each duct (sampled from various locations in the tumour to demonstrate typical features), the viable rim is clearly visible, with greatest proliferation along the outer edge. In the duct centres, necrotic cores are filled with partly-degraded nuclear debris (red arrows, pointing up and right), mostly-degraded nuclei (green arrow, pointing down and left), and possibly microcalcifications in the degraded region. Note the physical gap (black horizontal arrows) between the viable rims and the necrotic cores. (For interpretation of the references to colour in this figure legend, the reader is referred to the web version of this article.)

then this simplifies to

$$\frac{c_{cca}}{c_{ccr}} = \left(1-\frac{s}{2R}\right)^{n_{ccr}+1} \Bigg/ \left(1-\frac{s}{2R_A}\right)^{n_{cca}+1}. \tag{36}$$

This leaves a free parameter: in effect, $\langle \rho \rangle$ determines the equilibrium spacing but does not stipulate the time scale at which the forces operate to maintain the density. We apply our estimate of c_{ccr} (Supplementary material) to fully constrain the cell–cell mechanics. It may also be possible to constrain the mechanics by matching the simulation to the variance in ρ. Lastly, we can apply this technique in multiple tissue types and regions if the cell–cell mechanics were expected to vary (e.g., decreased cell–cell adhesion in hypoxic regions).

Cell–BM mechanics: If $c_{cba} \le c_{cca}$, too many cells pull away from the BM; this is not consistent with typical patient histopathology (Supplementary material); thus, we set $c_{cba} = 10c_{cca}$. Alternatively, one might obtain c_{cba} by measuring the mean distance between the cell centres and the BM and then setting $|\mathbf{F}_{cba}| = |\mathbf{F}_{cbr}|$ at that distance. For simplicity, we set $c_{cbr} = c_{ccr}$.

7. Sample calibration for Patient 100019

We demonstrate the calibration protocol on immunohistochemistry and histopathology data obtained from archived mastectomy tissue from an anonymised DCIS patient at the M.D. Anderson Cancer Center (anonymised case number 100019) from Edgerton et al. (2011). (Preliminary data may deviate from the final published values.) The patient had nuclear grade III (high-grade), mixed cribriform/solid-type DCIS with comedonecrosis; the patient measurements for this case (see below) are typical for mixed-type and solid-type cases in Edgerton et al. (2011). The measurement techniques for these data are detailed in Edgerton et al. (2011). In addition to these data, we measured the size of several nuclei in the viable rims in Fig. 6. The measurements for this case are given in Table 2. Note that the variation in patient data is the combined effect of measurement errors and genuine intratumoural heterogeneity.

This case had no measurements of f, so we approximate it as solid-type with $f \approx 1$. We set the patient-independent parameters as determined in Section 5. By applying the calibration protocol in Section 6 to these values and the patient-specific data, we obtain the parameter values in Table 1.

Table 2
Key data for anonymised case 100019 from Edgerton et al. (2011).

Quantity	Measurement (mean ± std. dev.)	Units
Duct radius R_{duct}	170.11 ± 76.37	μm
Viable rim thickness T	76.92 ± 12.51	μm
PI	17.43 ± 9.25	%
Raw AI	0.638 ± 0.424	%
Corrected AI	0.831 ± 0.553	%
Cell density ρ	0.003213 ± 5.95e−4	cells/μm²
Nuclear diameter $2R_N$	8.48–12.70 (typical range)	μm

Table 3
Verification of the patient-specific calibration: comparison of the patient (second column) and computed (third column) mean and standard deviation for the proliferative index, apoptotic index, viable rim thickness, and cell densities. All computed quantities are within the range of patient variation.

Quantity	Patient data	Simulation
PI (%)	17.43 ± 9.25	24.04 ± 4.587
Corrected AI (%)	0.831 ± 0.572	0.7378 ± 0.7146
Viable rim thickness (μm)	76.92 ± 12.51	80.73 ± 1.10
Cell density (cells/μm²)	0.003213 ± 5.95e−4	0.002950 ± 6.09e−5

All measurements given as mean ± standard deviation.

7.1. Verification of the calibration

To verify the calibration, we ran a simulation using the numerical methods in Section 4 for 30 days. We computed the simulated AI and PI, mean viable rim thickness, and viable rim cell density at 1-h increments for the last 15 days of simulated time. (The full time-course evolution is examined in Section 8.) C++ post-processing source code, simulation data for 0, 15, 30, and 45 days, and documentation are provided in the Supplementary material and at MathCancer.org (see footnote 3).

In Table 3, we present the mean and standard deviation of these computations for the last 15 days of the simulation and compare to the patient data; these are plotted in Fig. 7 as intervals [mean−std. dev., mean+std. dev.], for the simulated data (left bars) and actual patient data (right bars). Because apoptosis is a rare stochastic event ($< 1\%$) in a region with fewer than 500 cells, we expect considerable variability; indeed, this is observed in the patient AI as well. Because all the numerical targets (outlined in Table 2) are within the range of patient variation, the calibration

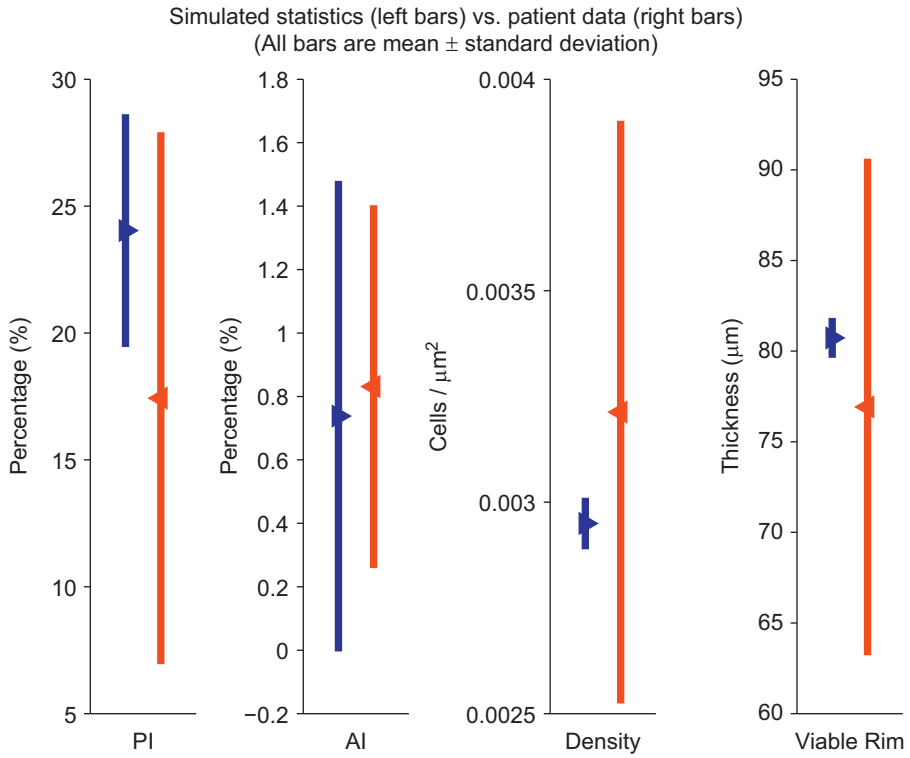

Fig. 7. *Verification of the patient-specific calibration*: we compare the simulated (left bars) and patient (right bars) PI (column one), AI (column two), cell density (column three), and viable rim thickness (column four) over the last 15 days of our simulation. Notice that the bars overlap for each datum, and the simulated means (left triangles) are within the patient variation for each datum. Hence, the calibrated model matches the calibration data within tolerances.

can be considered as successful. The discrepancy in the PI can be eliminated by better accounting for the length of G_1 in the calibration; see the Supplementary material.

8. Patient-calibrated DCIS simulation: hypothesis testing and model validation by clinical data

We now simulate DCIS in patient 100019 using the patient-independent parameters in Section 5; the patient-specific parameters are as in Section 6. The dynamic simulation is presented in Fig. 8. In this and all subsequent figures, small dark circles are cell nuclei, pale blue cells are quiescent ($\mathcal{Q}$), green cells are cycling ($\mathcal{P}$), red cells are apoptosing ($\mathcal{A}$), dark grey cells are necrotic but not yet lysed ($\mathcal{N}$), and the dark circles in the duct centres are necrotic cellular debris. The shade of red indicates the degree of calcification; bright red circles are clinically-detectable microcalcifications ($\mathcal{N}$ with $\tau > \tau_C$). An animation of this simulation is available as Video 1 in the Supplementary material (see footnote 3).

8.1. Overall spatiotemporal dynamics

In the simulation, a small initial population begins proliferating into the duct (0 days). As the tumour grows along the duct, oxygen uptake by the cells leads to the formation of an oxygen gradient (not shown). At 6.17 days, the oxygen level drops below σ_H in the centre of the duct near the leading edge of the tumour, causing the first instance of necrosis; this cell lyses at 6.42 days. By 7–14 days, a viable rim of nearly uniform thickness (approximately 80 μm) can be observed, demonstrating the overall oxygen gradient decreasing from σ_B at the duct boundary to σ_H at the edge of the necrotic core.

Consistent with the assumed functional form of the $\mathcal{Q} \to \mathcal{P}$ transition, proliferating cells are most abundant near the duct wall where the oxygen level is highest, with virtually no proliferation at the perinecrotic boundary. Because oxygen can diffuse into the tumour from the duct lumen, viable cells are also observed along the tumour's leading edge near the centre of the duct. Apoptosis occurs with approximately uniform distribution throughout the duct. See 7 days and onward in Fig. 8. These spatiotemporal dynamics emerge by 7–14 days and remain throughout the simulation. This is consistent with our analysis of the cell state dynamics in the Supplementary material.

The first clinically-detectable microcalcification appears at 21.17 days. By 22 days, a new characteristic length emerges: the trailing edge of the microcalcification maintains a distance of approximately 180 μm from the end of the duct. (See 28 days in Fig. 8 and Video 1 in the Supplementary material (see footnote 3).) Several features combine to cause this. We do not model contact inhibition, and so cells at the end of the duct continue to proliferate and push cells towards the tumour's leading edge. Because the end of the duct has reached a local dynamic equilibrium by this time, a steady flux of tumour cells into the necrotic region has emerged. Because the calcification time (τ_C) is fixed, the cells are pushed a fixed distance along the necrotic core before lysing and calcifying, leading to the observed "standing wave" pattern.

The necrotic core biomechanics play a key role in these dynamics. Whenever a necrotic cell lyses, its former volume is converted to a small core of cellular debris and a large pocket of (released) fluid, which is easily occupied by other cells. Thus, necrotic cell lysis acts as a mechanical stress relief, analogously to the mechanical pressure sink terms used in the necrotic core in Macklin and Lowengrub (2005, 2006, 2007, 2008). A pattern of cell flux emerges, where proliferating cells on the outer edge of the duct push interior cells towards the necrotic core, diverting much of the overall cell flux inwards rather than towards the tumour leading edge. See Video 1 in the Supplementary material (see footnote 3). This is a characteristic emergent feature of our model, and it has important implications for the rate of tumour advance. See Section 8.2.

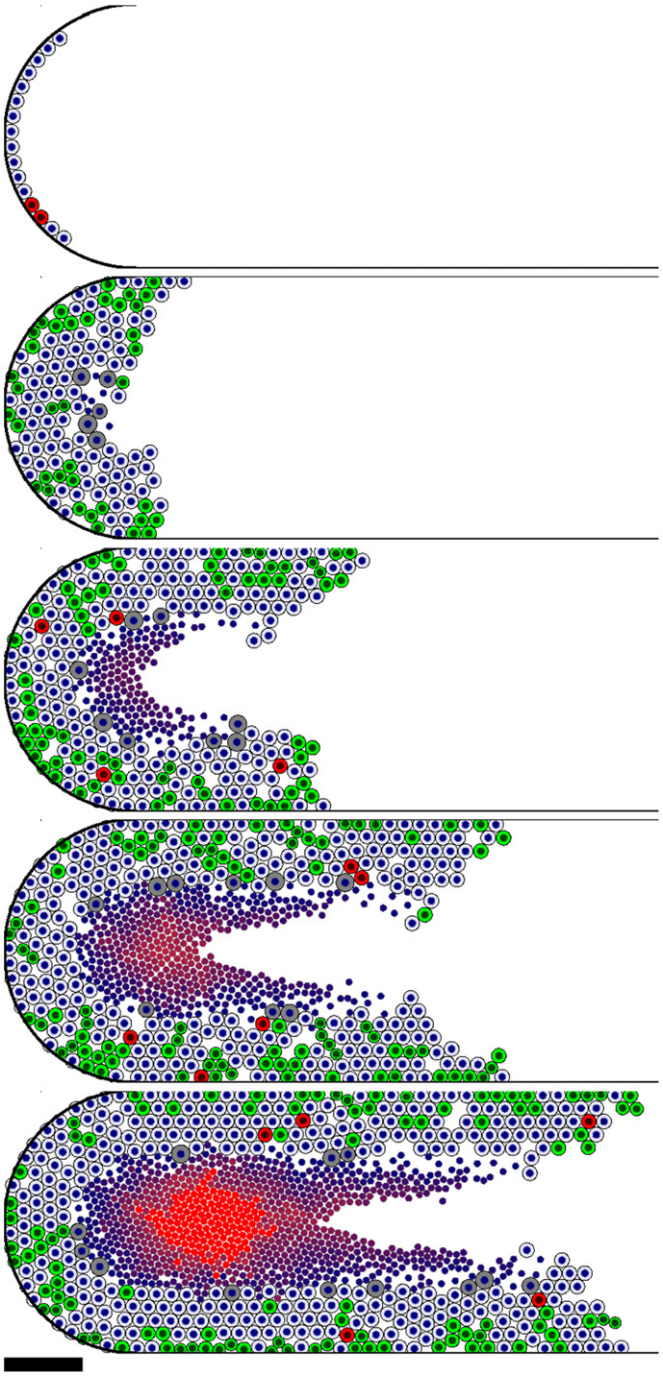

Fig. 8. *Agent-based simulation of DCIS in a* 1 *mm length of duct.* Legend: the black curve denotes the basement membrane. Cell nuclei are the small dark blue circles, quiescent cells ($\mathcal{Q}$) are pale blue, proliferating cells ($\mathcal{P}$) are green, apoptosing cells ($\mathcal{A}$) are red, and necrotic cells ($\mathcal{N}$) are grey until they lyse, after which their solid fraction remains as debris (dark circles in centre of duct). The shade of red in the necrotic debris indicates the level of calcification; bright red debris are clinically-detectable microcalcifications ($\mathcal{N}$ with $\tau > \tau_C$). *Simulated times* (from top to bottom): 0, 7, 14, 21, and 28 days. *Bar*: 100 μm. (For interpretation of the references to colour in this figure legend, the reader is referred to the web version of this article.)

A notable feature is the physical tear or gap between the tumour's viable rim and the necrotic core. (See 14 days and onward in Fig. 8.) This phenomenon is observed in stained tissue slides. See Fig. 6 and Section 8.4. It has been attributed to dehydration, but it was unclear whether the dehydration is an artifact due to tissue processing or a natural part of necrosis. The emergence of this phenomenon in a mechanistic model supports the hypothesis that the observed separation, while perhaps exacerbated during specimen preparation, is a *bona fide* result of DCIS tissue biomechanics. We note that an earlier version of our model—where necrotic cells gradually lost volume, rather than abruptly lysing—did not predict large gaps (Macklin et al., 2009a, 2010b). Fast cell swelling (over the course of $\tau_{NL} = 6$ h) and subsequent bursting act as a perturbation of the perinecrotic tumour boundary. This is consistent with our earlier hypothesis that the physical gap must be due in part to necrotic cell volume loss over a fast time scale (Macklin et al., 2009a).

8.2. Constant rate of tumour advance—confirmation with clinical data

To quantify and understand the tumour's growth, we post-processed our data to obtain the time evolution of the maximum position (extent) of viable tumour cells along the duct ($x_V(t)$) and the maximum position of the calcification ($x_C(t)$). To obtain better statistics on the growth dynamics, we extended our virtual duct to 1.5 mm, and continued the simulation to 45 days. C++ post-processing source code and pre-compiled binaries are provided in the Supplementary material (see footnote 3) to compute these and other statistics.

In Fig. 9, we plot x_V (top curve) and x_C (bottom curve) for the first 45 days of growth. For the first 10–11 days, the simulation exhibits transient dynamics due to the left computational boundary. After this time, the tumour has developed a sufficiently large region between the left boundary and the leading edge for the dynamics to begin reaching a steady state as discussed above. See 11 days in Fig. 10. From 11 to 45 days, x_V increases linearly at 27.97 μm/day (obtained by least-squares linear fitting); see the lighter line in Fig. 9. The constant rate of tumour advance is due to the combined effects of substrate transport limitations and necrotic cell lysis in the duct interior. Because lysis acts as a mechanical stress relief, a significant portion of the proliferative cell flux is directed towards the duct interior, rather than towards the leading edge. Hence, the only forward-directed flux occurs along the leading tumour edge. In additional simulations, we found that setting $\tau_{NL} = 15$ days results in convex, exponential-like growth curves (Supplementary material). This further supports the vital role of necrotic cell lysis in linear

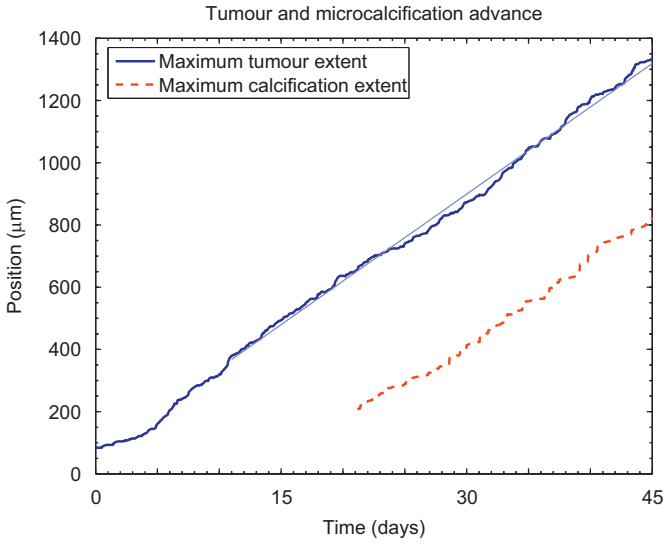

Fig. 9. *Tumour and microcalcification positions in the duct*: the top curve plots the maximum position of viable tumour tissue; the bottom curve plots the maximum calcification position. The lighter line is the least-squares fit of the tumour advance from 11 to 45 days.

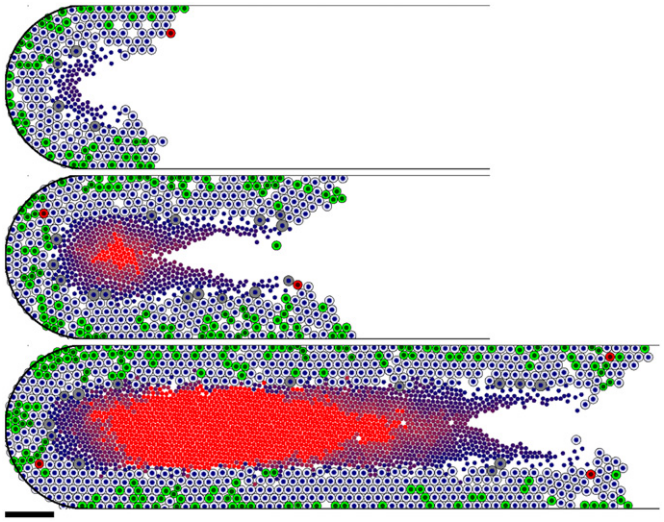

Fig. 10. *Additional timepoints for the baseline simulation*: from top to bottom, 11, 24, and 45 days. Cells are coloured as in Fig. 8. *Bar*: 100 μm. (For interpretation of the references to colour in this figure legend, the reader is referred to the web version of this article.)

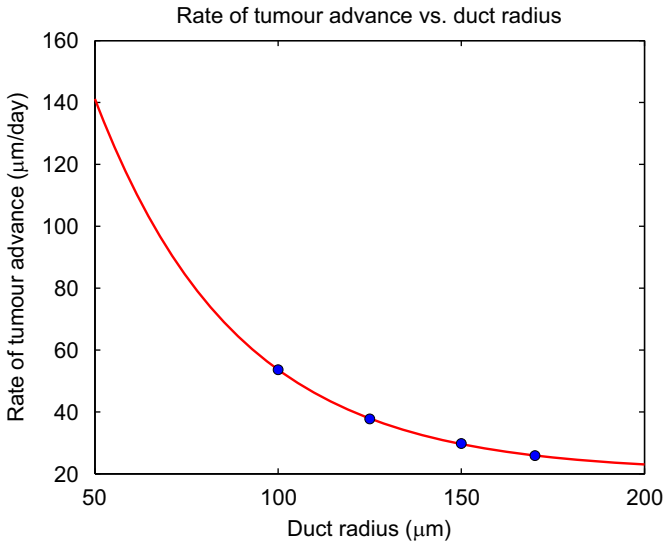

Fig. 11. *Inverse correlation of the duct radius and rate of tumour advance*: for small ducts, little lumen is available for mechanical relaxation, leading to rapid tumour advance. Conversely, growth is slower for larger ducts, with a threshold minimum rate of advance (approximately 20.52 μm/day). The mean proliferative and apoptotic indices were fixed for all simulations. (For interpretation of the references to colour in this figure legend, the reader is referred to the web version of this article.)

DCIS growth. Interestingly, recent modelling by Astanin and Preziosi (2009) with inverted geometry—a blood vessel surrounded by a growing tumour cord—also predicted linear tumour advance along the nutrient source.

Linear growth is consistent with mammographic measurements; Carlson et al. (1999) analysed the relationship between the maximum DCIS diameter and the elapsed time between mammograms, finding a near-linear relationship between the elapsed time between mammograms and the median DCIS size.

The rate of tumour advance in the duct—27.97 μm/day, or 10.2 mm per year—is consistent with DCIS growth estimates obtained by analysis of mammograms. Thomson et al. (2001) analysed changes in microcalcifications in mammograms to determine that high-grade DCIS tends to grow at about 7.1 mm per year (along an axis to the nipple). The group also analysed the data published by Carlson et al. (1999) and determined 13 mm/year and 6.8 mm/year mean and median growth rates, respectively. Simulating with $\tau_{G1} = 1$ min (for a better fit to the patient $\langle PI \rangle$—see the discussion in the Supplementary material) yields a rate of tumour advance of 7.86 mm/year (result not shown). It is encouraging that a mechanistic cell-scale model—with calibration solely by molecular- and cell-scale data—can accurately predict emergent, macroscopic behaviour.

8.2.1. Inverse relationship between duct radius and rate of tumour advance

The link between necrotic cell lysis and linear DCIS growth suggests that the rate of tumour advance is inversely correlated with the duct radius—larger ducts have a greater "reservoir" of lumen available for mechanical stress relief, thereby directing more cell flux into the lumen. Smaller ducts should exhaust this mechanism more quickly, leading to a faster overall advance.

To test this, we simulated DCIS with the same phenotypic parameters as our main simulation, in virtual ducts with $R_{duct} \in \{100, 125, 150, 170.11\}$. To eliminate the effect of differing oxygenation, we set the boundary condition σ_B to maintain $\langle \sigma \rangle$ (and hence $\langle PI \rangle$) constant in each simulation, as given in Eq. (29). All simulations had $\langle PI \rangle$ between 22 and 24%, and mean viable rim thicknesses between 80 and 81 μm (result not shown).

For the duct of radius 100 μm, cells reach the edge of the computational domain at 1 mm after just 20.58 days, with a mean rate of advance (from 10 to 20 days) of 53.65 μm/day. For the duct of radius 125 μm, cells reach 1 mm by 27 days, and advance 37.75 μm/day (from 10 to 27 days). For the 150 μm duct, the tumour advanced 29.80 μm/day (from 10 to 30 days). In our baseline case with radius 170.11 μm, cells advance at 25.87 μm/day from 10 to 30 days. See Fig. 11; these data suggest a relationship of the form

$$x'_V = a + e^{b - cR_{duct}}, \tag{37}$$

for positive constants a, b, and c. To estimate these, we chose a that minimises $\|x'_V - (a + e^{-p_a(R_{duct})})\|_2$ on $\{100, 125, 150, 170.11\}$, where $p_a(R_{duct})$ is the linear least-squares fit to $\ln(x'_V - a)$. By this procedure, we estimate

$$x'_V \approx 20.52 + e^{6.085 - 0.02584 R_{duct}} \text{ μm/day}. \tag{38}$$

See the red fitted curve in Fig. 11. Notice that as $R_{duct} \uparrow \infty$, the rate of tumour advance (for fixed oxygenation and cell phenotypic parameters) saturates at a nonzero minimum (estimated here at approximately 20.52 μm/day, or 7.5 mm per year). This has important implications for clinical planning, as it provides a range as well as a lower bound for the rate of growth of DCIS.

8.3. Calcification size and tumour size are linearly correlated—confirmation with clinical data

Prior to breast-conserving surgery, surgeons use mammographic images of microcalcifications to plan the correct surgical volume; for impalpable lesions, the planning is guided by stereotactically-placed localisation wires. Pathologists evaluate the success of the resection by examining the *surgical resection margin*: the outer edge of the excised specimen. The definition of an adequate margin width for DCIS (the distance from the tumour boundary to the surgical margin) varies by guideline. Smaller margin widths typically correlate with a greater risk of local recurrence (Boland et al., 2003; Macdonald et al., 2006). However, the goal of breast-conserving surgery is to minimise the amount of normal tissue that is excised while fully eliminating the DCIS. Several studies have addressed these competing goals to determine an adequate post-operative radiation field based on

margin width and other tumour characteristics (e.g. Vicini et al., 2004). However, there has been little attention given to improving the pre-operative estimate of the optimal surgical volume.

To investigate this, we define a "mammographic image error" $e(t) = x_V - x_C$ to be the distance between the edge of the viable tumour (x_V) and the edge of a radiographically detectable calcification (x_C). If the desired margin width per institutional surgical protocols is added to $e(t)$, then the distance from visible DCIS-associated microcalcifications to the desired surgical margin can be estimated from a mammographic image. (This requires that the microcalcifications are confirmed to arise from DCIS and are not benign.)

We found that from 21.17 days (the time of the first microcalcification) to 45 days, $e(t)$ grows at a slow, roughly linear rate. When attempting to fit $e(t)$ to the form $e_\infty - e^{a-rt}$ (for $e_\infty, a, r > 0$), we found no evidence that e reaches e_∞ in time scales under 4 years (results not shown). We conclude that x_V and x_C are linearly correlated over clinically-relevant time scales. See Fig. 12 left. This relationship is confirmed in the clinical literature. de Roos et al. (2004) compared the maximum calcification diameter in mammograms (corresponds to x_C) with the measured pathologic tumour size (corresponds to x_V) in 87 patients, finding a significant linear correlation between these measurements.

To predict the quantitative relationship between the mammographic and pathologic tumour sizes, we compute the linear least-squares fit between x_V and x_C

$$x_V \approx 0.4203 + 1.117 x_C \text{ mm}. \tag{39}$$

We plot this against our simulated DCIS data (blue points) and the data (red squares) from de Roos et al. (2004) in Fig. 12 right. Our model not only correctly predicts a linear correlation between a DCIS tumour's mammographic and pathologic sizes, but also demonstrates an excellent agreement with published clinical data *two orders of magnitude larger* than our simulation data.

de Roos et al. (2004) obtained a different linear fit ($x_V = 0.55 + 0.86 x_C$ mm) via linear regression analysis; the discrepancy is largely due to the greater number of outliers in the clinical data: seven of 87 cases had mammography–pathology discrepancies exceeding 2 cm. While we cannot extract all 87 data points from the published figure in de Roos et al. (2004) (25 points overlap), extracting the 62 non-overlapping points and excluding the seven outliers yields a least-squares fit ($x_V = 0.320 + 0.934 x_C$ mm) that better matches our prediction. Including the overlapping data points would likely further improve the match.

8.4. Predicted necrotic core microstructure—comparison with histopathology

The microstructure of the simulated necrotic core affords us further opportunity to generate hypotheses on DCIS, which can be tested by comparison against histopathology. In Fig. 13, we highlight several typical DCIS cross sections in our simulation at time 45 days.

In *Slice a*, there is a viable rim of thickness comparable to the remainder of the tumour, but with little visible evidence of necrosis. This suggests that in cases where too few ducts are sampled, a pathologist may fail to observe comedonecrosis, potentially changing the patient's Van Nuys Prognostic Index score (Silverstein et al., 1996) and treatment, whereas the biological mechanisms (particularly hypoxia) are the same as those with necrosis. This would be particularly true in cases where $\langle \text{PI} \rangle / \tau_P \approx \langle \text{AI} \rangle / \tau_A$, as little net cell flux from the viable rim to the necrotic core would be expected.

Farther from the tumour leading edge in *Slice b*, we see a ring of necrotic debris, surrounding a hollow duct lumen. In cross sections like this, there has not yet been sufficient tumour cell flux from the viable rim to completely fill the lumen with necrotic debris. Farther still from the leading edge in *Slice c*, there has been sufficient cell flux to fill the lumen with necrotic material; we also see an outermost band of intact necrotic nuclei, encircling a central region of mostly degraded nuclei (modelled here simply as partly calcified). Ducts like these are observed in our patient's H&E stains (Duct 1 in Fig. 14).

Farther from the leading edge in *Slice d*, a thin outermost band of relatively intact necrotic nuclei surrounds an inner band of mostly degraded necrotic material and an inner core of microcalcification. Similar cross sections are seen in our patient (Duct 1 in Fig. 14; left duct in Fig. 6). In *Slice e*, the microcalcification is larger, and the outermost band of intact necrotic nuclei is largely gone; see Ducts 2 and 3 in Fig. 14. The necrotic core is increasingly calcified with distance from the tumour leading edge.

The model predicts an age-ordered necrotic core microstructure, with oldest material in the centre surrounded by increasingly newer, less-degraded, and less-calcified material. This ordering—which

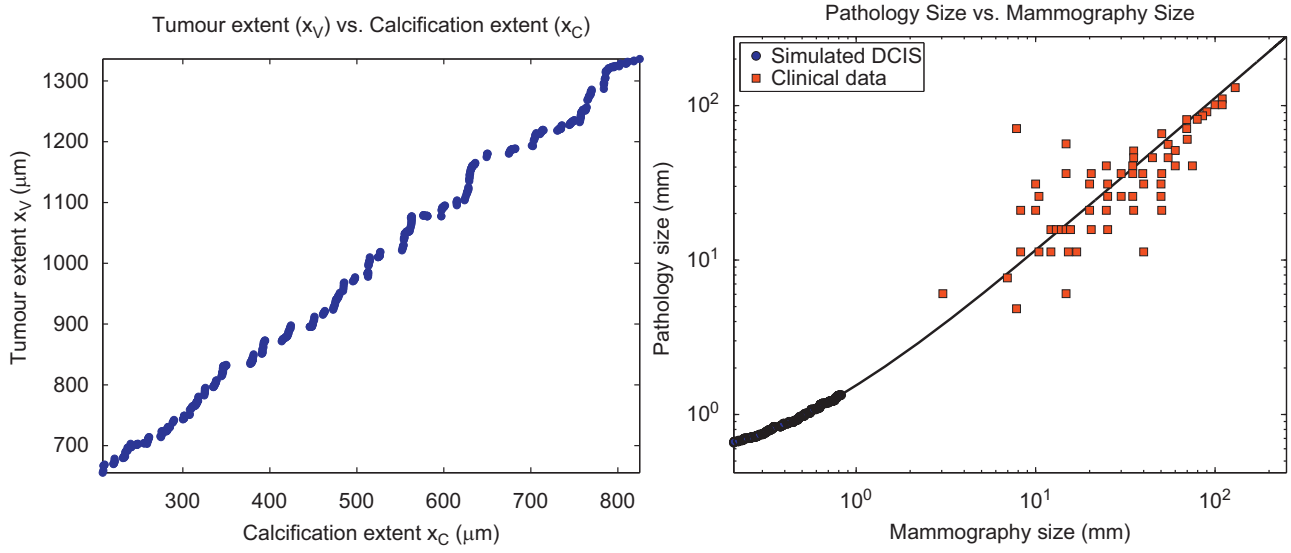

Fig. 12. *Comparison of mammographic and pathologic DCIS sizes*: *Left*: our DCIS simulation predicts a linear correlation between the mammographic calcification size (x_C) and the actual pathology-measured tumour size (x_V). *Right*: a linear least-squares fit of our simulation data (blue circles) fits clinical data (red squares) from de Roos et al. (2004), further demonstrating our model's predictivity. (For interpretation of the references to colour in this figure legend, the reader is referred to the web version of this article.)

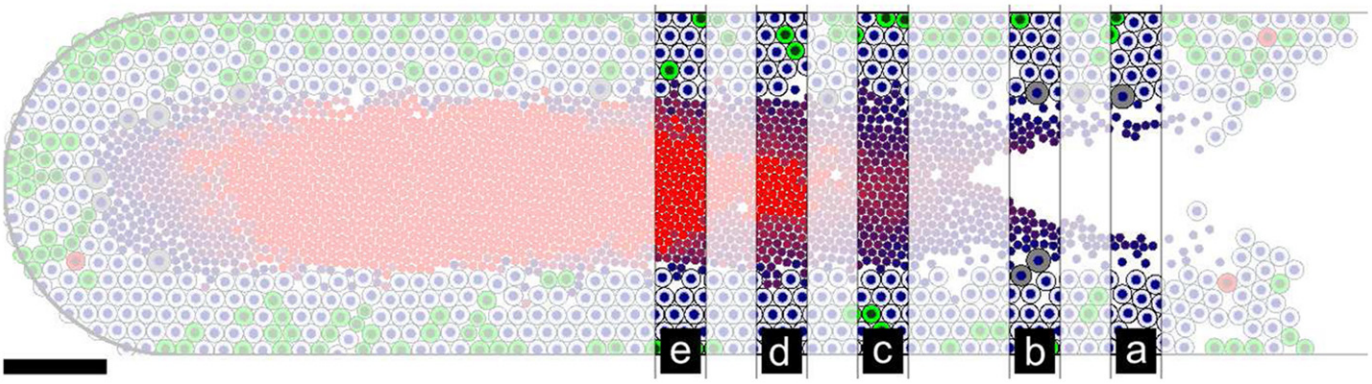

Fig. 13. *Selected DCIS cross-sections at 45 days.* (a) Close to the leading edge, very little necrotic debris is visible, although the viable rim thickness is comparable to other cross sections. (b) Farther from the leading edge, a band of intact necrotic debris surrounds a hollow duct lumen. (c) As the distance increases, the lumen is filled with necrotic debris. Nuclei on the outer edge is newer and less degraded; material in the centre is more degraded. (d) Farther still, a band of degraded nuclei surrounds a calcified core. (e) With increasing distance, the microcalcification occupies a greater portion of the necrotic core. *Bar* 100 μm. Cells are coloured as in Fig. 8. (For interpretation of the references to colour in this figure legend, the reader is referred to the web version of this article.)

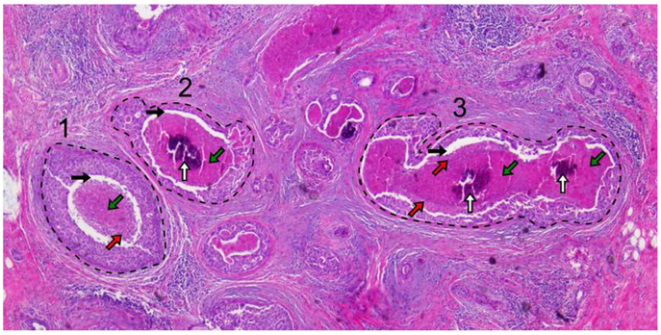

Fig. 14. *H&E staining of DCIS in several ducts* in case 100019. In each labelled duct, a readily visible outer viable rim (with faintly haematoxylin-stained nuclei) is separated from the necrotic core by a physical gap (black horizontal arrows). *Duct 1 necrotic core*: an outer band of partly degraded nuclei (red arrow, pointing up and right) surrounds a region of partly- or mostly-degraded nuclei (green arrow, pointing down and left). *Duct 2 necrotic core*: a region of mostly-degraded nuclei (green arrow, pointing down and left) surrounds a microcalcification (white vertical arrow). *Duct 3 necrotic core*: an outer band of partly degraded nuclei (red arrows, pointing up and right) surrounds a region of partly- or mostly-degraded nuclei (green arrows, pointing down and left), with a central core of microcalcifications (vertical white arrows). This duct is likely the intersection of two or more ducts near a branch point. (For interpretation of the references to colour in this figure legend, the reader is referred to the web version of this article.)

arises due to the overall flux of cells from the viable rim into the necrotic core—suggests that there is an additional necrosis time scale, separating the rates of necrotic nuclear degradation and calcification. As an initial estimate, we might surmise that nuclear degradation occurs on the time scale comparable to our current estimate of τ_C, and calcification may be somewhat slower than our initial estimate.

9. Discussion and ongoing work

In this work, we developed and analysed an agent-based model of ductal carcinoma in situ (DCIS) of the breast. Our model refines and makes more explicit the biological underpinnings of current agent-based cell models, particularly for finite cell–cell interaction distances, the need for partial cell overlap to account for uncertainty in cell positions and morphology, and a rigorous way to vary phenotypic transition probabilities with the time step size, the cell's internal state, and the microenvironment. We provide the most detailed necrosis model to date—including the impact of volume changes over time scales ranging from hours to weeks. We are the first to model necrotic cell calcification.

We developed the first patient-specific model calibration protocol to use pathology measurements from a *single time point* to simulate cancer in *individual patients*—an advance that could improve patient-tailored surgical and therapeutic planning. The calibration technique is broadly applicable to current agent-based models for multiple cancer types. Our model made numerous quantitative predictions on DCIS that we tested against clinical data. The simulated DCIS grows at a constant rate of approximately 1 cm per year (7.5–10.2 mm per year). These findings are quantitatively consistent with the clinical literature. The predicted difference between the mammographic and pathological tumour size increases slowly with time. Our model generates a linear correlation between the mammographic and pathological tumour sizes that quantitatively fits clinical data spanning several orders of magnitude. Observing such an excellent agreement over a broad range of scales suggests that the model mechanics are biologically sound, and that our parameter estimates (including order-of-magnitude estimates) are sufficiently accurate to allow quantitative biological and clinical investigations.

The model also correctly predicts the DCIS microstructure: a proliferative rim (with greatest proliferation on its outer edge) surrounds a stratified necrotic core. The viable rim and necrotic core are mechanically separated by a small gap—a feature that emerges from the mechanics of necrotic cell swelling and fast lysis, rather than being wholly attributable to tissue processing artifacts. The necrotic core has a layered structure that closely correlates with the "age" of the material. Relatively intact necrotic nuclei are observed in the outermost regions where cells have recently lysed. Closer to the duct centre, these nuclei start to disappear, and microcalcifications are found in the innermost region. These features are all observed in patient images, as illustrated in Fig. 14.

Biological insight: Because the standard deviations of the patient data are not used for calibration, we can use the simulated variation to test the model's underlying biological hypotheses. Because the simulated variation in PI is significantly lower than the actual variation (Fig. 7), the heterogeneity in DCIS proliferation is likely due to signalling variations (e.g., contact inhibition), rather than oxygenation gradients alone. On the other hand, the simulated and actual standard deviations in AI are quite similar (Fig. 7), supporting our biological hypothesis that apoptosis occurs at a low "background" rate that is independent of oxygenation and any other signalling. The patient's mean and standard deviation are of comparable magnitude, consistent with the exponentially-distributed random variables used in our model.

Necrotic core biomechanics drive DCIS development. The constant rate of tumour advance is due to the combined effects of substrate transport limitations and the mechanical stress relief provided by cell lysis in the necrotic centre. Remarkably, we recover a quantitatively reasonable growth rate without modelling contact inhibition. Galle et al. (2005) used a rigorously-calibrated agent model to assess the impact of contact inhibition and growth substrate transport limitations on 2-D and 3-D cell cultures, finding that contact inhibition alone was responsible for growth limitations in 2D, but substrate transport limitations are significant in 3D. They found that cell–cell contact inhibition is further reduced when cells lose contact with the BM. This is consistent with cells growing in a lumen, as in DCIS. More recently, Galle et al. (2009) further validated their agent model by comparing its predictions to a well-calibrated multiphase (continuum) model, with excellent model agreement in predicting 2-D *in vitro* Widr cell colony growth as a function of contact inhibition (where oxygen transport limitations do not apply). Their results—also consistent with continuum models such as Chaplain et al. (2006) that include ECM-MMP dynamics that are typical of DCIS microinvasions—show the importance of including contact inhibition signalling in future model refinements. Indeed, we found that proliferation varies with density, suggesting that contact inhibition shapes the finer details of DCIS progression (Macklin et al., 2010a).

The gap between the viable rim and the necrotic core is due to the relatively fast time scale of necrotic cell lysis. Analysis of the morphology and size of this gap may give insight on the *in vivo* progression of necrotic cell swelling and lysis, as well as the relative adhesive properties of lysed necrotic cells. The stratified necrotic core structure emerges due to the net outflux of cells from the viable rim into the necrotic core, resulting in an age structuring, and the relatively slow time scale of cell calcification. The relative distribution of these structures within the necrotic core may shed further insight as to the relative magnitudes of the time scales of pyknosis (nuclear degradation), water loss following lysis, and calcification. Indeed, the existence of a layer where the nuclei are mostly degraded with little evidence of calcification suggests that the time scale of pyknosis is between that of lysis (hours) and calcification (weeks).

Interestingly, the model predicts a linear/casting-type calcification, where the calcification forms a long "plug" that fills the duct centre. Other calcification morphologies (e.g., fine pleomorphic) are not predicted by the biophysical assumptions of our model. While casting-type calcifications correlate with comedonecrosis (Stomper et al., 1989), they are only present in approximately 30%–50% of DCIS (Evans et al., 2010; Hofvind et al., 2011). Furthermore, casting-type calcifications can be absent from small, high-grade DCIS, while present in larger, low-grade DCIS (Evans et al., 2010). Thus, additional biophysics (e.g., secretions, heterogeneous adhesive properties, and degradation of the calcifications over very long time scales) are required to model the broader spectrum of observed calcifications in DCIS. Our H&E images support the notion of long-time degradation. The centres of many calcifications—which we have shown are the "oldest" necrotic material—demonstrate significant cracks that suggest extensive degradation and weak cohesion. See Fig. 14.

Phospholipids—such as those from subcellular structures that likely form a "backbone" for the formation of microcalcifications—degrade with half-lives on the order of 80 (Ayre and Hulbert, 1996) to 300 h (Krause and Beamer, 1974) in non-pathologic tissue. If the degradation is 2–10 times slower in necrotic tissue, we would expect degradation to progress over the course of a few months. This may partly explain rare cases of spontaneous resolution of calcifications in mammograms, where calcifications become smaller or occult without alternative explanations (e.g., invasive foci) (Seymour et al., 1999): in slow-growing DCIS (e.g., with both high PI and AI, as is observed in high-grade DCIS, Buerger et al., 2000), calcifications may be degraded more quickly than they are replaced by new necrotic material.

Clinical insights: The growing difference between mammographic and pathologic sizes likely prevents using a single fixed "safe" surgical margin for all affected tumour ducts for all times. Instead, the margin size should vary with the tumour pathological properties, the duct size, oxygenation, and time. Given proper calibration to accurate measurements of a patient's proliferative and apoptotic indices, cell density, duct sizes, and other histopathologic and radiologic data, it should be possible to create a patient-specific map between the microcalcification geometry and the actual tumour shape and size. This could allow surgeons to use modelling based on data from the diagnostic core biopsy to more precisely plan DCIS surgical margins while removing less non-cancerous tissue, and could improve targeting of intra- and post-operative radiotherapy. Our calibration protocol can be combined with upscaling methods to calibrate multiscale models. As a proof of concept, we applied this approach to histopathology data from 17 patients to calibrate a simplified continuum model of DCIS, with the goal of predicting surgical excision volumes in individual patients (Edgerton et al., 2011). Although the continuum model used a steady state simplification and neglected necrosis, the predicted volumes were consistent with patient mammographic measurements in 14 of 17 cases. Hence, there is great promise in using our agent model and patient-specific calibration to incorporate patient pathology data into multiscale models.

The model predicts a general trend for the cross-sectional structure of a DCIS tumour. Moving from the basement membrane towards the duct centre, we see the following layers: a viable rim with greatest proliferation towards the basement membrane, a gap between the viable rim and necrotic core, an outer band of the necrotic core with relatively intact necrotic nuclei, an inner necrotic band of relatively degraded nuclei, and a central core of microcalcification. Cross sections closer to the leading edge contain fewer of these elements. We hypothesise that the microstructure of a given duct cross section in a histopathology slide could be used to estimate its position relative to the leading tumour edge in that duct; this could be tested by comparing the slide's position to any known geometric information on the patient's tumour. Moreover, if we can obtain sharper estimates of the various necrosis time scales, then we could potentially use the model to quantitatively predict the distance from each histopathology cross section to the actual tumour boundary, thereby further assisting surgical and therapeutic assessment.

Ongoing work: We chose DCIS as our initial modelling test bed because it is clinically and scientifically significant in and of itself, it is tractable to patient-specific simulation with currently-available data, and it is a necessary step in modelling progression to invasive ductal carcinoma (IDC). We plan to integrate molecular-scale models of hypoxia and invasion-related pathways (e.g., HIF-1α and the ErbB family), BM deformation and degradation, and motility. These additions will allow us to extend our investigations to IDC. Given the critical role played by necrosis in determining the DCIS growth rate, we are extending our model to better account for changes in the fluid and solid content, including pyknosis (nuclear degradation). The calcification model will be refined to describe the formation and degradation of calcium crystals in phospholipids (e.g., in degraded organelles) that remain after pyknosis. These improvements will be accompanied by advances in the model calibration to account for variations in the cell size throughout the cell cycle.

A potential weakness of this work is a lack of *unicity* in the data used for parameterisation, with *in vitro* and *in vivo* data combined

from human and animal models, across multiple cell types. This may result in subtle incompatibilities, such as inconsistencies in the cell microenvironments, and variations in key biophysical processes. In effect, the assumption that cells use the same fundamental processes with altered frequency may only hold to leading order, and may affect the quantitative accuracy of our model predictions. We are addressing this concern by conducting appropriate *in vitro* experiments to measure single-cell properties in breast cell lines (in various phenotypic states), and are reviewing the state-of-the-art in cell biomechanics experiments.

We are working to further validate the model and bring it closer to clinical application. We are refining the calibration protocol to better recapitulate the input PI and density data. We are conducting a patient-specific model validation, where we obtain pathology from multiple patients, determine the model-predicted growth rates and correlations between mammographic and pathology sizes, and compare these to the case histories and mammograms. We plan to leverage our early model successes to study the impact of inadequate surgical margins on tumour regrowth and microinvasion, and the effect of adjuvant chemo- and radiotherapy in ameliorating these phenomena.

Final thoughts: Our model is based upon physical conservation laws, with the key molecular and cellular biology of DCIS integrated through constitutive relations. We have taken care to not prescribe DCIS behaviour; these instead become manifest as *emergent phenomena*—a trait of a scientifically sound predictive model. By carefully calibrating the model, we can use its quantitative predictions to gain insight into the *underlying mechanisms* of DCIS. This is a key advance over phenomenological and statistical models, which can make predictions on DCIS behaviour but not on the underlying mechanisms. Furthermore, because statistical models generate correlations that apply to broad classes of patients, they cannot make quantitative predictions on DCIS in specific patients. Mechanistic models, on the other hand, have this potential. We have demonstrated that a carefully-calibrated, mechanistic model of DCIS can make quantitative, testable predictions at the macroscopic scale, based solely upon microscopic, patient-specific measurements. Once validated and integrated into highly-efficient hybrid multiscale modelling frameworks (Lowengrub et al., 2010; Deisboeck et al., 2011; Edgerton et al., 2011), this work has the potential to improve the precision, disease-focused, and cosmetic outcome of patient-tailored breast-conserving surgery and radiotherapy.

Acknowledgments

We thank: the Cullen Trust for Health Care (VC, MEE, PM) for generous support; the National Institutes of Health (NIH) for the Physical Sciences Oncology Center grants 1U54CA143907 (VC, PM) for Multi-scale Complex Systems Transdisciplinary Analysis of Response to Therapy—MC-START, and 1U54CA143837 (VC, PM) for the Center for Transport Oncophysics; the NIH for the Integrative Cancer Biology Program grant 1U54CA149196 (VC, PM) for the Center for Systematic Modeling of Cancer Development; and finally the National Science Foundation for grant DMS-0818104 (VC). PM is grateful for funding under the European Research Council Advanced Investigator Grant (ERC AdG) 227619, "M5CGS–From Mutations to Metastases: Multiscale Mathematical Modelling of Cancer Growth and Spread".

We thank the Division of Mathematics at the University of Dundee and the School of Biomedical Informatics at the University of Texas Health Science Center-Houston for generous computational support and resources. We appreciate assistance from Yao-Li Chuang (U. of New Mexico) for accessing data from Edgerton et al. (2011). PM thanks John Lowengrub (U. of California-Irvine), Hermann Frieboes (U. of Louisville), Dirk Drasdo (INRIA Rocquencourt/Paris), James Glazier and Maceij Swat (Indiana U.), and Mark Chaplain and Andrew Evans (U. of Dundee) for useful discussions. We thank the reviewers for their thoughtful questions that improved the quality of this manuscript.

Appendix A. Supplementary material

Supplementary data associated with this article, including animations, simulation data, open source C++ code, and further implementation and parameter information, can be found in the online version of 10.1016/j.jtbi.2012.02.002, with maintained versions at http://www.MathCancer.org/JTB_DCIS_2012/.

References

Abbott, R.G., Forrest, S., Pienta, K.J., 2006. Simulating the hallmarks of cancer. Artif. Life 12 (4), 617–634.

American Cancer Society, 2007. American Cancer Society breast cancer facts and figures 2007–2008. American Cancer Society, Inc., Atlanta.

Astanin, S., Preziosi, L., 2009. Mathematical modelling of the warburg effect in tumour cords. J. Theor. Biol. 254 (4), 578–590.

Ayre, K.J., Hulbert, A.J., 1996. Dietary fatty acid profile influences the composition of skeletal muscle phospholipids in rats. J. Nutr. 126 (3), 653–662.

Bankhead III, A., Magnuson, N.S., Heckendorn, R.B., 2007. Cellular automaton simulation examining progenitor hierarchy structure effects on mammary ductal carcinoma *in situ*. J. Theor. Biol. 246 (3), 491–498.

Boland, G.P., Chan, K.C., Knox, W.F., Roberts, S.A., Bundred, N.J., 2003. Value of the Van Nuys prognostic index in prediction of recurrence of ductal carcinoma *in situ* after breast-conserving surgery. Br. J. Surg. 90 (4), 426–432.

Buerger, H., Mommers, E.C., Littmann, R., Diallo, R., Brinkschmidt, C., Poremba, C., Dockhorn-Dworniczak, B., van Diest, P.J., Böcker, W.B., 2000. Correlation of morphologic and cytogenetic parameters of genetic instability with chromosomal alterations in situ carcinomas of the breast. Am. J. Clin. Pathol. 114, 854–859.

Butler, L.M., Khan, S., Rainger, G.E., Nash, G.B., 2008. Effects of endothelial basement membrane on neutrophil adhesion and migration. Cell. Immun. 251 (1), 56–61.

Byrne, H.M., Drasdo, D., 2009. Individual-based and continuum models of growing cell populations: a comparison. J. Math. Biol. 58 (4–5), 657–687.

Cabioglu, N., Hunt, K.K., Sahin, A.A., Kuerer, H.M., Babiera, G.V., Singletary, S.E., Whitman, G.J., Ross, M.I., Ames, F.C., Feig, B.W., Buchholz, T.A., Meric-Bernstam, F., 2007. Role for intraoperative margin assessment in patients undergoing breast-conserving surgery. Ann. Surg. Oncol. 14 (4), 1458–1471.

Carlson, K.L., Helvie, M.A., Roubidoux, M.A., Kleer, C.G., Oberman, H.A., Wilson, T.E., Pollack, E.W., Rochester, A.B., 1999. Relationship between mammographic screening intervals and size and histology of ductal carcinoma in situ. Am. J. Roentgenol. 172 (2), 313–317.

Chaplain, M., Graziano, L., Preziosi, L., 2006. Mathematical modelling of the loss of tissue compression responsiveness and its role in solid tumour development. Math. Med. Biol. 23 (3), 197–229.

Chen, L.L., Zhang, L., Yoon, J., Deisboeck, T.S., 2009a. Cancer cell motility: optimizing spatial search strategies. Biosystems 95 (3), 234–242.

Chen, W.W., Schoeberl, B., Jasper, P.J., Niepel, M., Nielsen, U.B., Lauffenburger, D.A., Sorger, P.K., 2009b. Input–output behavior of ErbB signaling pathways as revealed by a mass action model trained against dynamic data. Mol. Syst. Biol. 5 (1), 239 ff.

Cheng, L., Al-Kaisi, N.K., Gordon, N.H., Liu, A.Y., Gebrail, F., Shenk, R.R., 1997. Relationship between the size and margin status of ductal carcinoma in situ of the breast and residual disease. J. Natl. Cancer Inst. 89 (18), 1356–1360.

de Roos, M.A.J., Pijnappel, R.M., Post, W.J., de Vries, J., Baas, P.C., Groote, L.D., 2004. Correlation between imaging and pathology in ductal carcinoma in situ of the breast. World J. Surg. Oncol. 2 (1), 4.

Deisboeck, T.S., Wang, Z., Macklin, P., Cristini, V., 2011. Multiscale cancer modeling. Annu. Rev. Biomed. Eng. 13, 127–155.

Dillon, M.F., McDermott, E.W., O'Doherty, A., Quinn, C.M., Hill, A.D., O'Higgins, N., 2007. Factors affecting successful breast conservation for ductal carcinoma in situ. Ann. Surg. Oncol. 14 (5), 1618–1628.

Dillon, R., Owen, M., Painter, K., 2008. A single-cell based model of multicellular growth using the immersed boundary method. In: Khoo, B.C., Li, Z., Lin, P. (Eds.), Contemporary Mathematics: Moving Interface Problems and Applications in Fluid Dynamics, vol. 466, pp. 1–15. AMS, Providence. ISBN 978-0-8218-4267-6 (Chapter 1).

Drasdo, D., 2005. Coarse graining in simulated cell populations. Adv. Complex Syst. 8 (2&3), 319–363.

Drasdo, D., Höhme, S., 2003. Individual-based approaches to birth and death in avascular tumors. Math. Comput. Model. 37 (11), 1163–1175.

Drasdo, D., Höhme, S., 2005. A single-scale-based model of tumor growth *in vitro*: monolayers and spheroids. Phys. Biol. 2 (3), 133–147.
Drasdo, D., Kree, R., McCaskill, J.S., 1995. Monte–Carlo approach to tissue cell populations. Phys. Rev. E 52 (6), 6635–6657.
Edgerton, M.E., Chuang, Y.-L., Macklin, P., Yang, W., Bearer, E.L., Cristini, V., 2011. A novel, patient-specific mathematical pathology approach for assessment of surgical volume: application to ductal carcinoma in situ of the breast. Anal. Cell. Pathol. 34 (5), 247–263.
Enderling, H., Anderson, A.R.A., Chaplain, M.A.J., Munro, A.J., Vaidya, J.S., 2006. Mathematical modelling of radiotherapy strategies for early breast cancer. J. Theor. Biol. 241 (1), 158–171.
Enderling, H., Chaplain, M.A.J., Anderson, A.R.A., Vaidya, J.S., 2007. A mathematical model of breast cancer development, local treatment and recurrence. J. Theor. Biol. 246, 245–259.
Evans, A., Clements, K., Maxwell, A., Bishop, H., Handby, A., Lawrence, G., Pinder, S.E., 2010. Lesion size is a major determinant of the mammographic features of ductal carcinoma *in situ*: findings from the Sloane project. Radiology 53 (3), 181–184.
Franks, S.J., Byrne, H.M., King, J.R., Underwood, J.C.E., Lewis, C.E., 2003a. Modelling the early growth of ductal carcinoma in situ of the breast. J. Math. Biol. 47 (5), 424–452.
Franks, S.J., Byrne, H.M., Mudhar, H., Underwood, J.C.E., Lewis, C.E., 2003b. Modelling the growth of comedo ductal carcinoma in situ. Math. Med. Biol. 20 (3), 277–308.
Franks, S.J., Byrne, H.M., Underwood, J.C.E., Lewis, C.E., 2005. Biological inferences from a mathematical model of comedo ductal carcinoma in situ of the breast. J. Theor. Biol. 232 (4), 523–543.
Frieboes, H.B., Lowengrub, J.S., Wise, S., Zheng, X., Macklin, P., Bearer, E.L., Cristini, V., 2007. Computer simulations of glioma growth and morphology. NeuroImage 37 (S1), S59–S70.
Galle, J., Loeffler, M., Drasdo, D., 2005. Modeling the effect of deregulated proliferation and apoptosis on the growth dynamics of epithelial cell populations in vitro. Biophys. J. 88 (1), 62–75.
Galle, J., Preziosi, L., Tosin, A., 2009. Contact inhibition of growth described using a multiphase model and an individual cell based model. Appl. Math. Lett. 22 (10), 1483–1490.
Gatenby, R.A., Smallbone, K., Maini, P.K., Rose, F., Averill, J., Nagle, R.B., Worrall, L., Gillies, R.J., 2007. Cellular adaptations to hypoxia and acidosis during somatic evolution of breast cancer. Br. J. Cancer 97 (5), 646–653.
Gov, N.S., Gopinathan, A., 2006. Dynamics of membranes driven by actin polymerization. Biophys. J. 90 (2), 454–469.
Hanahan, D., Weinberg, R.A., 2000. The hallmarks of cancer. Cell 100 (1), 57–70.
Hoehme, S., Drasdo, D., 2010. Biomechanical versus nutrient control: what determines the growth dynamics of mammalian cell populations. Math. Pop. Studies 17 (3), 166–187.
Hofvind, S., Iversen, B.F., Eriksen, L., Styr, B.M.S., Kjellevold, K., Kurz, K.D., 2011. Mammographic morphology and distribution of calcifications in ductal carcinoma *in situ* diagnosed in organized screening. Acta Radiol. 52 (5), 481–487.
Jemal, A., Siegel, R., Ward, E., Murray, T., Xu, J., Thun, M.J., 2007. Cancer statistics. Cancer J. Clin. 57 (1), 43–66.
Kerlikowske, K., Molinaro, A., Cha, I., Ljung, B.M., Ernster, V.L., Stewart, K., Chew, K., Moore II, D.H., Waldman, F., 2003. Characteristics associated with recurrence among women with ductal carcinoma in situ treated by lumpectomy. J. Natl. Cancer Inst. 95 (22), 1692–1702.
Kharait, S., Hautaniemi, S., Wu, S., Iwabu, A., Lauffenburger, D.A., Wells, A., 2007. Decision tree modeling predicts effects of inhibiting contractility signaling on cell motility. BMC Syst. Biol. 1, 9ff.
Kim, Y., Stolarska, M.A., Othmer, H.G., 2011. The role of the microenvironment in tumor growth and invasion. Prog. Biophys. Mol. Biol. 106 (2), 353–379.
Krause, R.F., Beamer, K.C., 1974. Lipid content and phospholipid metabolism of subcellular fractions from testes of control and retinol-deficient rats. J. Nutr. 104 (5), 629–637.
Lampejo, O.T., Barnes, D.M., Smith, P., Millis, R.R., 1994. Evaluation of infiltrating ductal carcinomas with a DCIS component: correlation of the histologic type of the in situ component with grade of the infiltrating component. Semin. Diagn. Pathol. 11 (3), 215–222.
Lowengrub, J.S., Frieboes, H.B., Jin, F., Chuang, Y.-L., Li, X., Macklin, P., Wise, S.M., Cristini, V., 2010. Nonlinear modeling of cancer: bridging the gap between cells and tumors. Nonlinearity 23 (1), R1–R91.
Macdonald, H.R., Silverstein, M.J., Lee, L.A., Ye, W., Sanghavi, P., Holmes, D.R., Silberman, H., Lagios, M., 2006. Margin width as the sole determinant of local recurrence after breast conservation in patients with ductal carcinoma in situ of the breast. Am. J. Surg. 192 (4), 420–422.
Macklin, P., Lowengrub, J.S., 2005. Evolving interfaces via gradients of geometry-dependent interior poisson problems: application to tumor growth. J. Comput. Phys. 203 (1), 191–220.
Macklin, P., Lowengrub, J.S., 2006. An improved geometry-aware curvature discretization for level set methods: application to tumor growth. J. Comput. Phys. 215 (2), 392–401.
Macklin, P., Lowengrub, J.S., 2007. Nonlinear simulation of the effect of microenvironment on tumor growth. J. Theor. Biol. 245 (4), 677–704.
Macklin, P., Lowengrub, J.S., 2008. A new ghost cell/level set method for moving boundary problems: application to tumor growth. J. Sci. Comp. 35 (2–3), 266–299.
Macklin, P., Kim, J., Tomaiuolo, G., Edgerton, M.E., Cristini, V., 2009a. Agent-based modeling of ductal carcinoma in situ: application to patient-specific breast cancer modeling. In: Pham, T. (Ed.), Computational Biology: Issues and Applications in Oncology. Springer, pp. 77–112. ISBN 978-1441908100 (Chapter 4).
Macklin, P., McDougall, S., Anderson, A.R.A., Chaplain, M.A.J., Cristini, V., Lowengrub, J., 2009b. Multiscale modeling and nonlinear simulation of vascular tumour growth. J. Math. Biol. 58 (4–5), 765–798.
Macklin, P., Edgerton, M.E., Cristini, V., 2010a. Agent-based cell modeling: application to breast cancer. In: Cristini, V., Lowengrub, J.S. Multiscale Modeling of Cancer, pp. 216–244. ISBN 978-0521884426 (Chapter 10).
Macklin, P., Edgerton, M.E., Lowengrub, J.S, Cristini, V., 2010b. Discrete cell modeling. In: Cristini, V., Lowengrub, J.S. Multiscale Modeling of Cancer, pp. 92–126. ISBN 978-0521884426 (Chapter 6).
Mannes, K.D., Edgerton, M.E., Simpson, J.F., Jenson, R.A., Page, D.L., 2002. Pagetoid spread in ductal carcinoma in situ: characterization and computer simulation. In: United States and Canadian Academy of Pathology (USCAP) Annual Meeting 2002, Chicago.
Norton, K.-A., Wininger, M., Bhanot, G., Ganesan, S., Barnard, N., Shinbrot, T., 2010. A 2D mechanistic model of breast ductal carcinoma in situ (DCIS) morphology and progression. J. Theor. Biol. 263 (4), 393–406.
Ottesen, G.L., Christensen, I.J., Larsen, J.K., Larsen, J., Baldetorp, B., Linden, T., Hansen, B., Andersen, J., 2000. Carcinoma in situ of the breast: correlation of histopathology to immunohistochemical markers and DNA ploidy. Breast Cancer Res. Treat. 60 (3), 219–226.
Owen, M.R., Byrne, H.M., Lewis, C.E., 2004. Mathematical modelling of the use of macrophages as vehicles for drug-delivery to hypoxic tumour sites. J. Theor. Biol. 226 (4), 377–391.
Page, D.L., Dupont, W.D., Rogers, L.W., Landenberger, M., 1982. Intraductal carcinoma of the breast: follow-up after biopsy only. Cancer 49 (4), 751–758.
Panorchan, P., Thompson, M.S., Davis, K.J., Tseng, Y., Konstantopoulos, K., Wirtz, D., 2006. Single-molecule analysis of cadherin-mediated cell–cell adhesion. J. Cell Sci. 119 (1), 66–74.
Ramis-Conde, I., Chaplain, M.A.J., Anderson, A.R.A., 2008a. Mathematical modelling of cancer cell invasion of tissue. Math. Comp. Model. 47 (5–6), 533–545.
Ramis-Conde, I., Drasdo, D., Anderson, A.R.A., Chaplain, M.A.J., 2008b. Modeling the influence of the e-cadherin-beta-catenin pathway in cancer cell invasion: a multiscale approach. Biophys. J. 95 (1), 155–165.
Rejniak, K.A., 2007. An immersed boundary framework for modeling the growth of individual cells: an application to the early tumour development. J. Theor. Biol. 247 (1), 186–204.
Rejniak, K.A., Anderson, A.R.A., 2008a. A computational study of the development of epithelial acini: I. Sufficient conditions for the formation of a hollow structure. Bull. Math. Biol. 70 (3), 677–712.
Rejniak, K.A., Anderson, A.R.A., 2008b. A computational study of the development of epithelial acini: II. Necessary conditions for structure and lumen stability. Bull. Math. Biol. 70 (5), 1450–1479.
Rejniak, K.A., Dillon, R.H., 2007. A single cell-based model of the ductal tumor microarchitecture. Comp. Math. Meth. Med. 8 (1), 51–69.
Ribba, B., Saut, O., Colin, T., Bresch, D., Grenier, E., Boissel, J.P., 2006. A multiscale mathematical model of avascular tumor growth to investigate the therapeutic benefit of anti-invasive agents. J. Theor. Biol. 243 (4), 532–541.
Sanders, M.E., Schuyler, P.A., Dupont, W.D., Page, D.L., 2005. The natural history of low-grade ductal carcinoma in situ of the breast in women treated by biopsy only revealed over 30 years of long-term follow-up. Cancer 103 (12), 2481–2484.
Seymour, H.R., Cooke, J., Given-Wilson, R.M., 1999. The significance of spontaneous resolution of breast calcification. Br. J. Radiol. 72 (853), 3–8.
Shraiman, B.I., 2005. Mechanical feedback as a possible regulator of tissue growth. Proc. Natl. Acad. Sci. USA 102 (9), 3318–3323.
Silva, A.S., Gatenby, R.A., 2010. A theoretical quantitative model for evolution of cancer chemotherapy resistance. Biol. Direct 5 (1), 25ff.
Silva, A.S., Gatenby, R.A., Gillies, R.J., Yunes, J.A., 2010. A quantitative theoretical model for the development of malignancy in ductal carcinoma *in situ*. J. Theor. Biol. 262 (4), 601–613.
Silverstein, M.J., 1997. Predicting residual disease and local recurrence in patients with ductal carcinoma in situ. J. Natl. Cancer Inst. 89 (18), 1330–1331.
Silverstein, M.J., Lagios, M.D., Craig, P.H., Waisrnan, J.R., Lewinsky, B.S., Colburn, W.J., Poller, D.N., 1996. A prognostic index for ductal carcinoma in situ of the breast. Cancer 77 (11), 2267–2274.
Smallbone, K., Gatenby, R.A., Gillies, R.J., Maini, P.K., Gavaghan, D.J., 2007. Metabolic changes during carcinogenesis: potential impact on invasiveness. J. Theor. Biol. 244 (2), 703–713.
Smith, J.A., Martin, L., 1973. Do cells cycle? Proc. Natl. Acad. Sci. USA 70, 1263–1267. 〈http://www.pnas.org/content/70/4/1263〉.
Sontag, L., Axelrod, D.E., 2005. Evaluation of pathways for progression of heterogeneous breast tumors. J. Theor. Biol. 232 (2), 179–189.
Stomper, P.C., Connolly, J.L., Meyer, J.E., Harris, J.R., 1989. Clinically occult ductal carcinoma in situ detected with mammography: analysis of 100 cases with radiologic–pathologic correlation. Radiology 172 (1), 235–241.
Talsma, A.K., Reedijk, A.M.J., Damhuis, R.A.M., Westenend, P.J., Vles, W.J., 2011. Re-resection rates after breast-conserving surgery as a performance indicator: introduction of a case-mix model to allow comparison between dutch hospitals. Eur. J. Surg. Onc. EJSO 37 (4), 357–363. doi:10.1016/j.ejso.2011.01.008.
Thomson, J.Z., Evans, A.J., Pinder, S.E., Burrell, H.C., Wilson, A.R.M., Ellis, I.O., 2001. Growth pattern of ductal carcinoma in situ (DCIS): a retrospective analysis based on mammographic findings. Br. J. Cancer 85 (2), 225–227.
Venkatesan, A., Chu, P., Kerlikowske, K., Sickles, E.A., Smith-Bindman, R., 2009. Positive predictive value of specific mammographic findings according to reader and patient variables. Radiology 250 (3), 648–657.

Vicini, F.A., Kestin, L.L., Goldstein, N.S., 2004. Defining the clinical target volume for patients with early-stage breast cancer treated with lumpectomy and accelerated partial breast irradiation: a pathologic analysis. Int. J. Radiat. Oncol. Biol. Phys. 60 (3), 722–730.

Wang, Z., Zhang, L., Sagotsky, J., Deisboeck, T.S., 2007. Simulating non-small cell lung cancer with a multiscale agent-based model. Theor. Biol. Med. Model. 4, 50ff.

Ward, J.P., King, J.R., 1997. Mathematical modelling of avascular tumour growth. IMA J. Math. Appl. Med. Biol. 14 (1), 36–69.

Wise, S.M., Lowengrub, J.S., Frieboes, H.B., Cristini, V., 2008. Three-dimensional multispecies nonlinear tumor growth—I. Model and numerical method. J. Theor. Biol. 253 (3), 524–543.

Yagata, H., Harigaya, K., Suzuki, M., Nagashima, T., Hashimoto, H., Ishii, G., Miyazaki, M., Nakajima, N., Mikata, A., 2003. Comedonecrosis is an unfavorable marker in node-negative invasive breast carcinoma. Pathol. Int. 53 (8), 501–506.

Zhang, L., Athale, C.A., Deisboeck, T.S., 2007. Development of a three-dimensional multiscale agent-based tumor model: simulating gene-protein interaction profiles, cell phenotypes and multicellular patterns in brain cancer. J. Theor. Biol. 244 (7), 96–107.

Zhang, L., Wang, Z., Sagotsky, J.A., Deisboeck, T.S., 2009. Multiscale agent-based cancer modeling. J. Math. Biol. 58 (4–5), 545–559.